Comparison of Currents derived from X-band Radar and collected In-situ Data in Ameland Inlet

Florian Grossmann

MSc Thesis

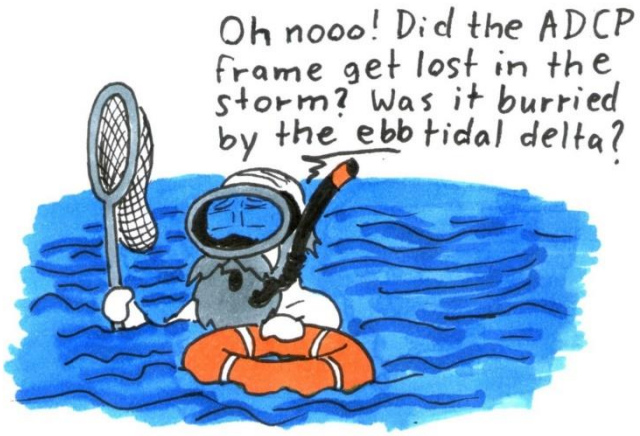

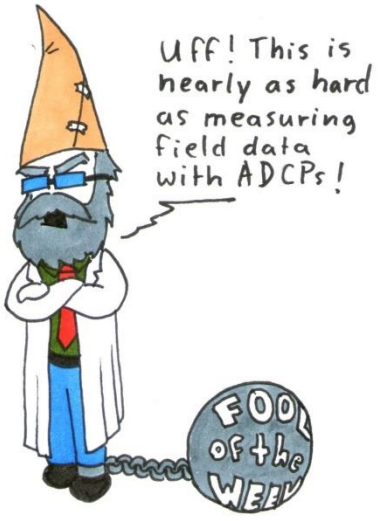

TU Delft

CoMEM

Deltares
Enabling Delta Life

Cover page by Phrittenbude.

ERASMUS +: ERASMUS MUNDUS MOBILITY PROGRAMME

Master of Science in

COASTAL AND MARINE ENGINEERING AND MANAGEMENT

CoMEM

Comparison of Currents derived from X-band Radar and collected In-situ Data in Ameland Inlet

Technische Universiteit (TU) Delft
Delft, The Netherlands
10 July 2019

Florian Grossmann

The Erasmus+: Erasmus Mundus MSc in Coastal and Marine Engineering and Management is an integrated programme including mobility organized by five European partner institutions, coordinated by Norwegian University of Science and Technology (NTNU).

The joint study programme of 120 ECTS credits (two years full-time) has been obtained at two or three of the five CoMEM partner institutions:

- Norges Teknisk- Naturvitenskapelige Universitet (NTNU) Trondheim, Norway
- Technische Universiteit (TU) Delft, The Netherlands
- Universitat Politècnica de Catalunya (UPC). BarcelonaTech. Barcelona, Spain
- University of Southampton, Southampton, Great Britain
- City University London, London, Great Britain

During the first three semesters of the programme, students study at two or three different universities depending on their track of study. In the fourth and final semester an MSc project and thesis has to be completed. The two-year CoMEM programme leads to a multiple set of officially recognized MSc diploma certificates. These will be issued by the universities that have been attended by the student. The transcripts issued with the MSc Diploma Certificate of each university include grades/marks and credits for each subject.

Information regarding the CoMEM programme can be obtained from the programme coordinator:

Øivind A. Arntsen, Dr.ing.
Associate professor in Marine Civil Engineering
Department of Civil and Environmental Engineering
NTNU Norway
Mob.: +4792650455 Fax: + 4773597021
Email: oivind.arntsen@ntnu.no

CoMEM URL: https://www.ntnu.edu/studies/mscomem

CoMEM Thesis

This thesis was completed by:
Florian Grossmann

Under supervision of:

Prof. dr. ir. Stefan G. J. Aarninkhof (Chair)	*TU Delft*
Dr. ir. Sierd de Vries	*TU Delft*
Dr. ir. Marion F.S. Tissier	*TU Delft*
Ir. Matthijs Gawehn	*TU Delft, Deltares*

As a requirement to attend the degree of:
Erasmus+: Erasmus Mundus Master in Coastal and Marine Engineering and Management (CoMEM)

Taught at the following educational institutions:

Norges Teknisk- Naturvitenskapelige Universitet (NTNU)
Trondheim, Norway

Technische Universiteit (TU) Delft
Delft, The Netherlands

University of Southampton,
Southampton, Great Britain

At which the student has studied from August 2017 to July 2019.

Acknowledgements / Danksagung

First, I would like to thank the CoMEM academic staff. I am aware of all the difficulties you go through to organize such a highly international program. Despite your busy schedules, you have always gone the extra-mile to make us feel at home. Thanks to Sonja Hammer, Øivind Asgeir Arntsen, Hachem Kassem, Robert Nicholls, Marcel Stive and Bas Hofland.

Second, I would like to thank my thesis committee members. I feel very privileged for the peak on the way your critical minds approach all the confusing problems research poses. Also, you made me feel part of the faculty very quickly and now it is very sad to leave. Thanks to Stefan Aarninkhof for sharing his experience and wisdom to keep this thesis on the right track at a crucial stage. Thanks to Marion Tissier for helping me to reflect on my research more critically (and for not being mad at me for winning at curling). Thanks to Sierd de Vries for his trust and for always putting the focus on my personal development and on advancing my academic skills. Thanks to Matthijs Gawehn whose curiosity and passion for research are contagious. I cannot imagine a better daily supervisor.

Third, I would like to thank all my international friends who have walked along with me for a few steps on this two-year Erasmus Mundus path. Each one of you has contributed to my personal development and I am hoping that our paths align once more in the future. Thanks to El Ri, Gréggy, Vera and Renan for the warmth in Norwegian winters. Thanks to Cassandra, Stuart, Alejandra, Nader, Chris, Tom, Charles, Albert, Inés and Michelle for the steady advice in a windy first semester in Delft. Thanks to Toby, Jay, Erfan, Célie, Nes, Jack, Paul and Mole for the laddism in a very un-laddish Southampton. Thanks to Alessandro, Akshay, Bas, Jochem, Luis, Susanna, Camila and Jo for the social backup in socially-isolating thesis madness.

Fourth, I would like to thank my dear CoMEM friends. Only very few people get to share an experience as special as the one we shared. While reinventing our daily lives every five to six months and studying at some of Europe's most demanding universities, sharing our experiences has always helped me to cope. Furthermore, the cultural inputs you have given me are a gift for a lifetime. Thanks to Mazen, Khaled, Sungsoo, Fahad, Nauman and Daniil for providing me with completely new perspectives on the world. Thanks to Lulu for sharing her positive energy and drive. Thanks to Ganga for her kind-heartedness and the courage to get up on that stage and do it! Thanks to Marlon for being himself – the gentlest person I know. Thanks to Nikos for all the great coffee breaks, barbecues and parties. Thanks to Ingrid for providing some female balance, for laughing at one or two of my jokes and for introducing me to the beauty of leather attire. Thanks to Hassan for the fantastic conversations and for teaching me many things about different kinds of culture (working, culinary, social, religious, and many more). Thanks to Matteo and Fred for all the good times, for tolerating my weird ways and for being true friends (also for accepting my Catan-dominance).

Fünftens möchte ich meinen engen Freunden, Bundesbrüdern und meiner Familie danken. Ohne Euch wäre dies alles nie und nimmer möglich gewesen. Ihr bietet mir einen schützenden Anker, wenn ich auf meinen Reisen in der großen weiten Welt drohe in einen Mahlstrom hineinzutreiben. Meinen Dank an Mechthild, weil sie beweist, dass Telefonstrippen noch besser als Ankerketten vor Mahlströmen schützen. Meinen Dank an meine lieben Bundesbrüder, weil, obwohl wir nicht immer einer Meinung sind, sie mein Leben auf vielfältige Art bereichern und Aachen mir immer eine zweite Heimat sein wird. Meinen Dank an meinen lieben Leibbursch, weil er für mich ein ganz besonderer Mensch und einfach auf der gleichen Wellenlänge ist. Meinen Dank an meine Großeltern, weil es mich zwar unglaublich schmerzt immer weg zu sein, ich mir ihrer offenen Arme aber immer sicher sein kann. Meinen Dank an meine Eltern, für die Liebe, mit der sie mich großgezogen haben, das bedingungslose Vertrauen, mit dem sie es mir ermöglichen mich frei zu entfalten, und dass ich weiß, ich kann immer nach Hause kommen.

Florian Grossmann

Delft, July 2019

Comparison of Currents derived from X-band Radar and collected In-situ Data in Ameland Inlet

Abstract: Velocities derived from X-band radar were compared to depth-averaged ADCP measurements in a complex tidal inlet system at Ameland, the Netherlands. Inclusion of depth-assimilation and ensemble-averaging in radar calculations led to smaller differences between ADCP and radar. The observed differences were clustered and related to water level elevations, wind velocities, wave periods, wave heights, spatial coherence in radar output and error metrics of the radar fitting procedure. Larger waves and higher wind velocities were observed to benefit radar agreement with ADCP results. Rising water levels benefitted agreement in east-west direction. Falling water levels benefitted agreement in north-south direction. Confidence intervals of the fitting procedure were observed to coincide with differences between ADCP and radar and potential for filtering based on them was shown. Nevertheless, an unclarified tendency towards northwestern bias, which may be specific to the comparison locations, remains. The radar at Ameland monitors the whole inlet system and provides current velocities everywhere in its range. This study shows that its currents are in good agreement with ADCP depth-averaged currents throughout most of the tidal cycle. Furthermore, it stresses radar's potential for better monitoring of the coast and for cost-effective coastal field measurements to obtain large datasets, even in hydrodynamically very complex regions.

Keywords: Remote Sensing, Coastal Field Measurements, Current Monitoring, Depth Inversion, X-Band Radar, SEAWAD, Kustgenese 2.0, XMFit

1 Introduction

The magnitude and direction of currents play an integral role in sediment dynamics and coastal morphology. To understand local morphodynamics, it is therefore valuable to measure currents. This can be done with in-situ or remote sensing techniques. In-situ measurements are costly due to the required man hours and equipment. Also, and despite their accuracy, common problems include the influence of carrying structures (Mueller, 2015) and the limited spatial coverage. Remotely-sensed current measurements are generally coarser than in-situ measurements but offer several advantages (Holman and Haller, 2013, Gangeskar, 2018): The equipment does not need to resist violent wave action in the surf zone; there is no danger to operators installing, repairing or retrieving equipment; and the equipment is not affected by scouring, burying or fouling. Moreover, remote sensing has the potential to provide measurements over larger areas at high temporal resolution and low cost.

In recent years, the interest for remote sensing in coastal engineering has been growing. Systems were developed to measure wave characteristics, wave dissipation, bathymetry and current vectors (Holman and Haller, 2013). A particular example, based on RAdio Detection And Ranging (RADAR), is the X-band MATLAB® Fitting (XMFit) algorithm (Friedman, 2014). It was developed at TU Delft and Deltares and it is a 3D-Fourier based method as proposed by Young et al. (1985a). It estimates both bathymetry and near-surface currents. Currently, it is used to monitor the morphodynamics of the Ameland ebb-tidal delta in the Netherlands for the Dutch coastal research project Coastal Genesis 2.0 (Gawehn et al., 2019 *in prep.*).

Remote sensing of currents via radar initially focused on High Frequency (HF) radar (Crombie, 1955). It is based on Bragg resonance of water waves with radio waves of similar wavelength (Valenzuela, 1978 and Nieto Borge et al., 2004). Even though HF radar is used operationally in the US (Terrill et al., 2006), the highest achievable current resolutions are *O*(1-6 km). X-band radar allows higher resolutions and the simultaneous estimation of depth. It is based on a broadband wavenumber-Doppler shift relationship instead of direct radio wave Doppler shifts, as HF radar is (Campana et al., 2016). Composite surface scattering theory (Bass et al., 1968) and Wright, 1968) confirmed that (in X-band radar) the emitted electromagnetic waves are being scattered by centimeter scale capillary waves riding on the water surface of large scale (longer) water waves. Subsequent research showed that the longer waves, on which capillary waves are riding, are modulating the backscattering characteristics of Bragg resonance from capillary waves (Plant and Keller, 1990, Wetzel,

1990, Lee et al., 1995). Therefore, the long waves become visible via their modulation of the signals that capillary waves scatter. Nieto Borge et al. (2004) identified three distinct processes of modulation.

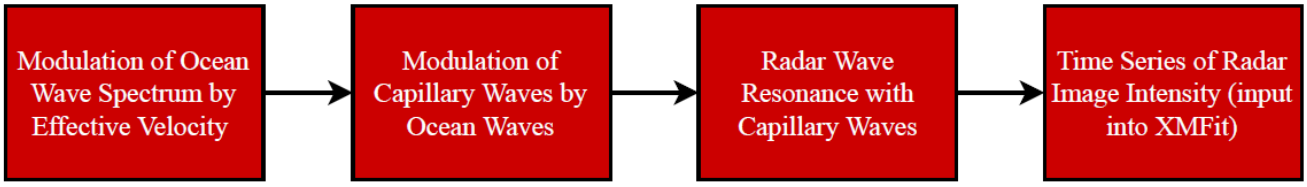

Figure 1 Flow chart describing the flow of information from effective velocity to input into XMFit as radar images.

Current estimation from radar, whether HF radar (e.g. Teague et al., 2001 and Trizna and Xu 2006) or X-band radar (e.g. Young et al., 1985b, Senet et al., 2008 and Hessner and Bell, 2009), commonly relies on the Doppler shift that currents apply to the ocean wave spectrum (Stewart and Joy, 1974). Stewart and Joy (1974) derived, under assumption of infinite depth, a relation between the Doppler shift-causing effective velocity $\boldsymbol{u_{eff}(k)}$ and the velocity profile $\boldsymbol{u(z)}$. Kirby and Chen (1989) extended their relation to finite depths (assuming profile shapes a priori):

$$\boldsymbol{u_{eff}}(\boldsymbol{k}) = \frac{2\boldsymbol{k}}{sinh(2\boldsymbol{k}h)} \int_h^0 \boldsymbol{u}\,(z)\cosh[2\boldsymbol{k}(h+z)]\,dz \quad (1)$$

Ha (1979), on the other hand, developed a method to estimate $\boldsymbol{u(z)}$ from Stewart and Joys' (1974) equation without a priori profile assumptions, recently implemented with success in X-band radar calculations of current shear (Campana et al., 2017).

Note that there is confusion over the physical significance of the effective velocity $\boldsymbol{u_{eff}(k)}$. Stewart and Joy (1974) stress that radar measures "…the weighted average of the current with depth,… ". Young et al. (1985b) highlight that the in-situ current profile originates from a superposition of tidal currents, ocean circulation currents, wind drift currents and wave-induced currents (including Stokes drift), acknowledging the complexity in calculating values for $\boldsymbol{u_{eff}(k)}$ and in comparing them to in-situ measurements. Senet et al. (2001) refer to $\boldsymbol{u_{eff}(k)}$ as the velocity of encounter, stressing that it is a near-surface current and noting that the vertical dimension of Doppler shifts originating from currents is limited to the penetration depth of ocean waves, being approximately half the waves' wavelengths. Campana et al. (2016) refer to $\boldsymbol{u_{eff}(k)}$ as "… a weighted depth-average effect currents have on the wavefield.", leaving room for interpretation which current the radar actually measures. Nevertheless, Young et al. (1985b), Senet et al. (2001) and Campana et al. (2016) inherently adopt Stewart and Joys' (1974) definition of effective velocity.

Equation (1) indicates that radar's depth-average is weighted according to wavenumber $\boldsymbol{k}$ and radar should measure currents up to a depth of $(2\boldsymbol{k})^{-1}$, equaling 8 % of the ocean wavelength (Figure 16). This was partly confirmed (Teague et al., 2001) but there is confusion over the in-situ validation of radar currents. Ludeno et al. (2016), Hessner et al. (2015) and Lund et al. (2015) compare X-band radar estimates to Lagrangian drifters, Acoustic Doppler Current Profiler (ADCP) depth-averages over the near-surface region and single ADCP bins at larger depth. Furthermore, radar currents represent large areas whereas ADCPs represent single locations and Lagrangian drifters represent single paths.

So far, the validation of XMFit has mainly focused on bathymetry. Only Weijenborg (2015) focused on XMFit radar currents but stresses the confusion over their physical meaning (and whether they include Stokes Drift or not). Thus, there is a need to determine what the relation of XMFit currents to in-situ currents is and how useful they can be in coastal monitoring applications. Furthermore, the reasons for observed differences between XMFit and in-situ currents must be identified and methods for reducing the differences must be developed.

To do so, depth-averaged currents from in-situ measurements are compared to XMFit currents under different calculation settings. It is observed how difference characteristics are related to the settings, environmental conditions and statistics of the fitting procedure to draw conclusions on their influence. Finally, the potential for output filtering and practical application of XMFit in coastal monitoring is tested.

2 Methodology

Results from a field campaign, conducted in September 2017, offered the opportunity to compare remote sensing-derived current estimates (from X-band radar) with in-situ data (from ADCP measurement frames) at the northern edge of Ameland inlet's Ebb Tidal Delta (ETD, Figure 2). In this study, environmental data, measured at nearby stations or estimated from numerical models, spatial coherence in radar output and error metrics of the radar method's fitting procedure are related to observed differences between ADCPs and radar. September 2017 was characterized by a combination of calm conditions and storm events (notably storm Sebastian peaking on September 13th).

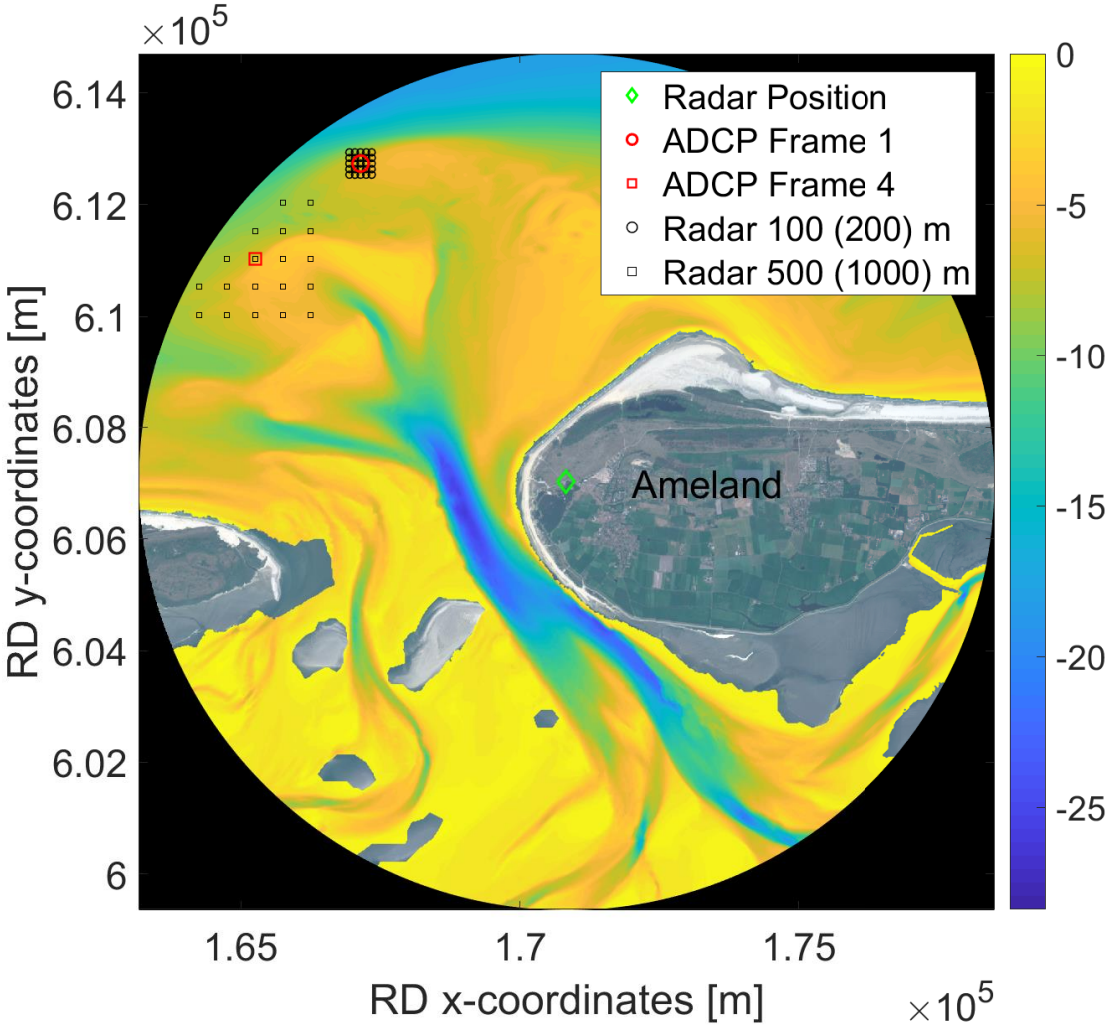

Figure 2 Satellite image of Ameland inlet georeferenced to Dutch Rijksdriehoekscoördinaten with image size corresponding to radar range. Depths superimposed from combined bathymetric surveys (February and September 2017) and indicated by colorbar on the right. Positions of radar (green diamond), ADCP frames (red circle and square) and radar calculation points at different spacings (black circles for small spacing and squares for large spacing) indicated by markers.

2.1 Radar Measurements

The radar used for data acquisition operates from the lighthouse at Ameland inlet. It has a range of 7.675 km but is cut off at 7.5 km in order to minimize the effect of inaccuracies at the boundary. The resolution of a single pixel is 7.5 m with one radar image containing 2048 such pixels. The framerate of the radar images is 2.85 s.

XMFit is based on the Doppler shifted linear dispersion relationship. Radar images of backscatter intensity are divided into computational cubes and stacked in time. Via application of a 3D-FFT (Fast Fourier Transform) the energy spectrum $E(k_x,k_y,\omega)$ is obtained (Young et al., 1985a). The image intensity dispersion shell in three-dimensional wavenumber-frequency space is then fitted to dispersion relationships. Depth and current information of the best-fitting theoretical dispersion shell are output. For more elaborate information on the theoretical basis of the algorithm, refer to the work of Gawehn et al. (2019 *in prep.*).

Radar results for velocity correspond to a weighted depth-average (Stewart and Joy, 1974). In this study, a spatial domain of roughly 0.92 km^2 is used to obtain a single depth-averaged velocity which is then compared to the ADCP velocity measured at the frame (Figure 3). Like the ADCP velocities, radar velocities are time averaged over intervals of 12 minutes – the intervals will be referred to as epochs. In each epoch, calculations are made at the ADCP frame location and surrounding points (Figure 3) because comparing multiple outputs provides a more resilient result. Many different spacings of calculation points were tested and the relation of two is shown schematically (Figure 3). Medians and means, of the velocities obtained in all calculation points, are used to select a single output velocity, representing the epoch. The spatial coherence of an epoch describes how similar output velocities in the calculation points (Figure 3) are. Even though XMFit can be run without depth input, the algorithm is first run in depth-assimilated mode to constrain the solution. A combined bathymetry from single beam surveys in February and September 2017 is used as ground truth depth.

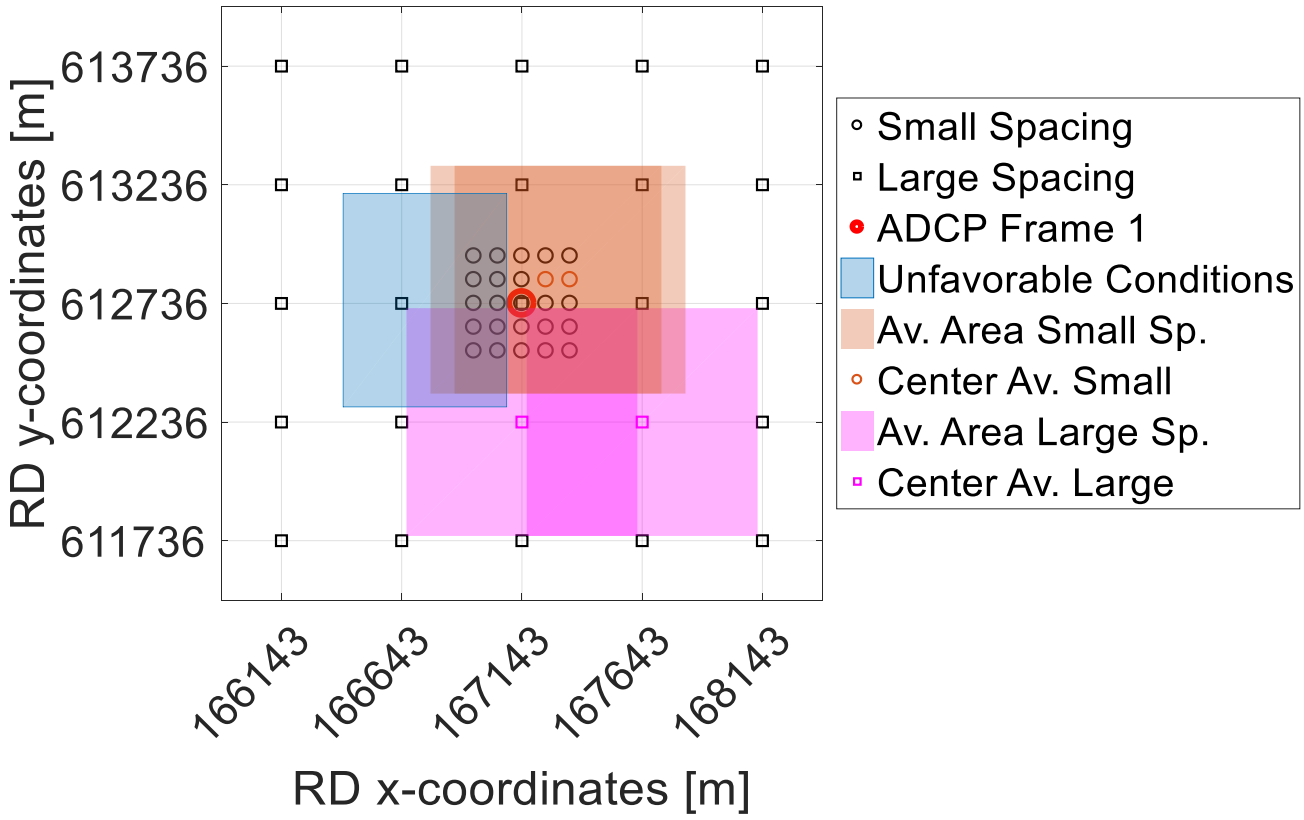

Figure 3 Schematization of calculation points (black circles and squares) for calculation of radar velocities (magnified from Figure 2 showing both grids for ADCP frame 1). Points surround the frame (red circle) in steps of 100 (200) m (small spacing) and 500 (1000) m (large spacing). Hypothetical region of unfavorable conditions shown (blue rectangle). The averaging area of two respective points in small and in large spacing is shown exemplarily (orange and magenta squares centered at orange and magenta markers).

XMFit does not output velocities if the fitting procedure violates error metric settings (e.g. $R^2 < 0.6$). Due to challenging environmental conditions, no XMFit output was produced in multiple days of the field campaign. Furthermore, the radar was damaged during storm Sebastian so that it was not operative between September 14th and 24th. Additionally, medians and means are only cal ulated and output if velocities were output in five or more calculation points. This limits the times of conjunct data availability, from ADCPs and radar, to 31.8.17 09:32 – 8.9.17 19:31, from now on referred to as time interval 1, and 26.9.17 02:29 – 30.8.17 19:29, from now on referred to as time interval 2. Note that in time interval 1 one radar output per hour but in time interval 2 two radar outputs per hour are used.

The medians of the most important error metrics of all calculation points per epoch are calculated and saved. This includes the Coefficient of Determination (R^2) and Root Mean Square Error (RMSE), representing the correlation between image intensity and theoretical dispersion shells, as well as directional confidence intervals, representing the uniqueness with which XMFit's Levenberg Marquardt algorithm selects the output directional current component.

2.2 ADCP Measurements

To enable a comparison with radar, ADCP measurements are depth averaged. Upward-looking Teledyne RDI Workhorse Monitor ADCPs gathered velocity data while downward-looking Nortek Aquadopp Current Meters measured pressures. The sensors were mounted onto stainless-steel frames and the frames were placed on the seabed. Under the assumption of hydrostatic pressure, the measured pressures are used to calculate the water surface elevation. With the obtained information, the ADCPs' submerged bins are delimited and velocity is assumed constant between uppermost bin and water surface. If at least three data points are available in the vertical profile, a Piecewise Cubic Hermite Interpolating Polynomial is fitted to the data points between lowest bin and a pre-defined point 0.48-0.7 m below the calculated water surface. The depth-integrated profile is divided by the distance between the lowest bin and the pre-defined point to obtain the depth-averaged velocity components (Figure 4, left panel).

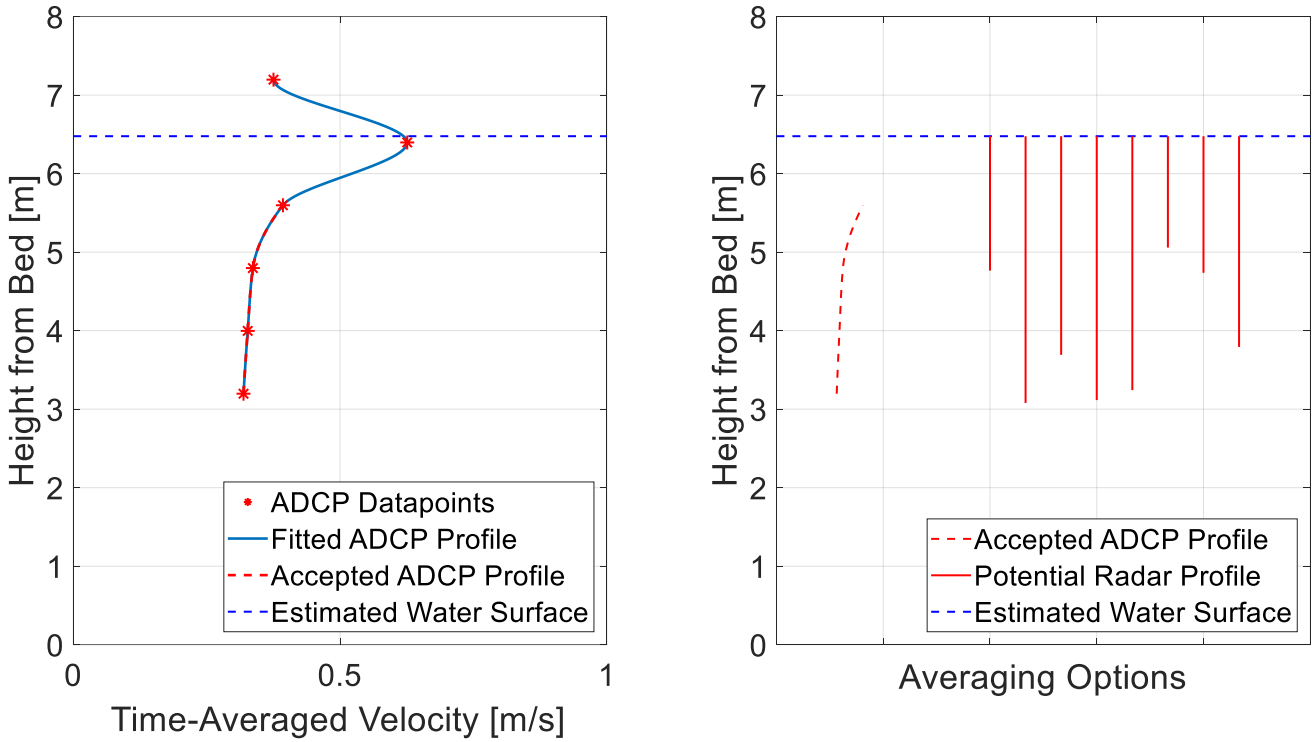

Figure 4 Left panel: Depth-averaging in ADCP measurements, showing the accepted section for averaging (red dashed line) of a profile (blue line) fitted to measured data points (red asterisks) in relation to the estimated water surface (blue dashed line). Right panel: Profile depth visible for ADCP (red dashed line) compared to potential profile depths visible for radar (red lines).

The pre-defined point is set because the assumption of hydrostatic pressure does not allow accurate calculation of the water surface (because of dynamic pressure from waves and currents amongst others). Furthermore, the profiles are frequently observed to bulge in the region of the estimated water surface (Figure 4, left panel). This may be linked to velocity contamination from waves or difficulties resulting from only partial submersion of the bin. Via the pre-defined point, the troublesome region of the profile is ignored and the upper parts of mainly logarithmic profiles are used (neglecting the bottom region and boundary layer). Note, however, that ADCP and radar are potentially averaging over different parts of the profile (Figure 4, right panel).

2.3 Environmental Measurements

Water level data are obtained from the tide gauge at Terschelling and from the pressure sensors on the ADCP frames. Wave parameters are obtained from Deltares's MATROOS visualization tool for Ameland Station 1-1. Wind data are obtained from station L91. For all environmental measurements, the stations, which represent conditions at the ADCP frames most accurately, are chosen. Data are retrieved in 1 h intervals corresponding to the end date of velocity-averaging epochs.

2.4 Comparison Procedure

ADCP and radar velocities are averaged over the same temporal domains. Spatially, the radar averages over a large horizontal area whereas the ADCP measurements represent a single location. The agreement in averaging depth is uncertain (Section 1 and Figure 4). Comparison of output velocities per epoch yields the difference between ADCP and radar and allows clustering of epochs according to difference characteristics. The comparison is conducted via the velocities' directional components in east-west and north-south.

The radar output velocity per epoch is selected as the mean or median over all calculation points per epoch. Error metrics, gauging the correlation of ADCP and radar velocities, are used to compare mean and median. The first metric is bias, representing the average difference between ADCP and radar output over the whole experiment. The second metric is the unbiased Root Mean Square Error (uRMSE), representing the random error (Entekhabi et al., 2014).

With ADCP frames 1 and 4 (Figure 2), the comparison is conducted at two locations on the ETD. Furthermore, the storm damage divides the time series of radar results into two time intervals. Thus, the available data are categorized as four different experiments. Experiment 1, representing frame 1 in time interval 1, is used to explain the analysis and show model examples of the results. Experiment 2, representing frame 1 in time interval 2, experiment 3, representing frame 4 in time interval 1, and experiment 4, representing frame 4 in time interval 4, are compared to experiment 1 and used to assess the general applicability of experiment 1's results.

The radar calculations are conducted with different depth-assimilation and calculation point settings (Figure 5). The obtained difference patterns with ADCP depth-averages are then correlated with environmental conditions, error metrics of the fitting procedure and spatial coherence in calculation points.

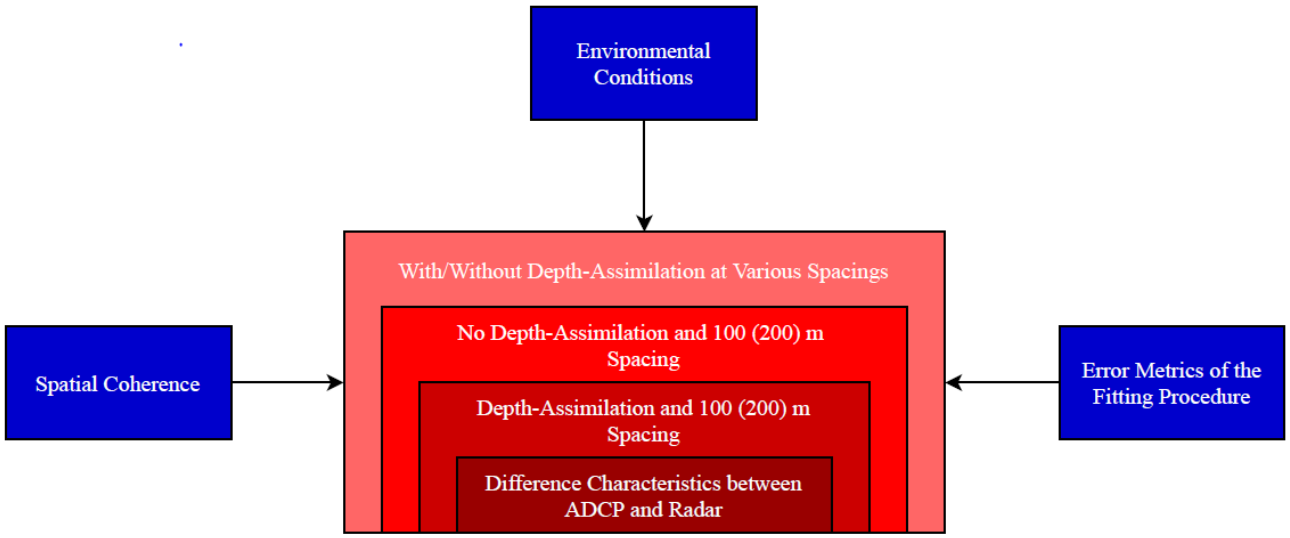

Figure 5 Flow chart of conducted calculations and comparisons.

3 Results

Radar velocities for comparison with ADCP measurements are calculated in multiple ways, always using ensemble-averaging over calculation points (spaced in steps of 100 (200) m in Sub-sections 3.1 and 3.2 (Figure 17, black circles) and spaced in various steps in Sub-section 3.3).

3.1 Base Case with Depth-Assimilation

ADCP current measurements conform to expected southeastern and northwestern flow directions (Elias, 2017) in the study area (Figure 9). The highest current magnitudes are observed in eastern direction. In addition to the radar-derived median, the radar-derived mean per epoch is shown in comparison to ADCP output (Figure 9). The mean has larger differences to the ADCP result than the median, which is confirmed in other experiments – also visible in the bias and uRMSE resulting from median and

mean. This is attributed to faulty outliers that affect the result more strongly in the mean. Therefore, the median is used for further analyses. It captures the changing directions throughout the tidal cycle except for some outliers. Epochs are clustered according to the relation of ADCP and radar outputs (Table 1).

According to differences between ADCP and radar, good (< 0.1 m/s) and bad epochs (> 0.5 m/s) are defined. In opposite direction epochs, ADCP and radar indicate opposite directions. Overshoot epochs are defined to feature radar estimating the maximum positive or negative velocity component magnitudes of the tidal cycle higher than observed by the ADCP. Type 1 (Type 2) outlier epochs are defined to feature surrounding epochs comparing well (not well) with the ADCP but single outlying epochs being subject to much larger (smaller) differences between ADCP and radar (e.g. Figure 9; epochs 18 (Type 1), 29 (Type 1), 36 (Type 2) and 89 (Type 1) in the east-west component and epochs 15 (Type 2), 29 (Type 2), 59 (Type 1), 69 and 70 (Type 2) in the north-south component).

Two striking error sources become visible. First, there are time periods where the radar is more susceptible to sudden fluctuations (random error) in output (e.g. Figure 9; epochs 14-47 in the east-west component). Such periods are also found in the other experiments and they are linked to high uRMSE. Note that the east-west component is always more susceptible than the north-south component (Table 1). This is attributed to the lower velocities in north-south components and allocation of spectral energy according to the dominant wave direction (on the northern side), constraining potential fits more effectively in north-south. Second, northwestern bias in the radar estimate leads to large differences between ADCP and radar (e.g. Figure 9; epochs 40-43 in the east-west component and epochs 71-80 in the north-south component). In the east-west component, bias significantly increases the number of bad epochs. Even though the calculated bias is generally smaller in the north-south component (Table 1), its impact is crucial as velocity magnitudes are low so that it leads to many opposite direction epochs, especially at times of southward velocity. This becomes clearly visible in all experiments apart from experiment 4, where less epochs of southward velocity were output (Table 1). Therefore, good correlation in the north-south component is mostly confined to northward directed currents.

Table 1 Bias and uRMSE between ADCP and radar for depth-assimilated calculations at spacing 100 (200) m. Clustered epochs shown component-wise and in percent of the total epochs with output in the experiment (which are shown in parentheses). Summation per experiment does not equal 100 % because certain clusters may overlap and not every epoch fulfills at least one of the clustering conditions.

Experiment		Bias [m/s]	uRMSE [-]	Good [%]	Bad [%]	Opposite [%]	Overshoot [%]	Outlier [%] (1 / 2)
Exp. 1 (90 epochs)	EW	-0.166	0.304	30.00	03.33	17.78	17.78	08.89 / 04.44
	NS	0.266	0.239	15.56	06.67	41.11	15.56	01.11 / 06.67
Exp. 2 (62 epochs)	EW	-0.443	0.473	06.45	27.42	20.97	30.65	04.84 / 20.97
	NS	0.151	0.174	33.87	00.00	41.94	16.13	01.61 / 09.68
Exp. 3 (57 epochs)	EW	0.041	0.608	19.30	15.79	22.81	22.81	21.05 / 17.54
	NS	0.186	0.417	19.30	17.54	36.84	15.79	15.79 / 21.05
Exp. 4 (25 epochs)	EW	-0.823	0.548	00.00	56.00	24.00	52.00	12.00 / 36.00
	NS	0.089	0.226	32.00	04.00	28.00	28.00	20.00 / 28.00

The experiments were conducted in different time intervals at different frames. In time interval 2 (experiments 2 and 4), bias in the east-west component is much larger than in time interval 1 (Table 1). This leads to few good epochs, many bad and overshoot epochs as well as a dominance of type 2 outliers (which indicates that good epochs are not consecutive). In the north-south component, bias and uRMSE decrease in time interval 2. This does not affect the clustered epochs as significantly as observed for the east-west component and is attributed to the lower velocity magnitudes in time interval 2. Generally, time interval 2 is characterized by more outliers than time interval 1. At frame 4 (experiments 3 and 4), a substantial increase in uRMSE, coinciding with decreases in good epochs and increases in bad epochs and outliers, becomes visible in both components (Table 1). Furthermore, less epochs with output are available at frame 4. These specific issues at frame 4 are attributed to larger bathymetric gradients and closer proximity to the border of the radar domain, complicating image analysis and acquisition. Potentially, they may also result from the position of the frames relative to the ebb chutes (Figure 1) and local flow processes.

3.2 Without Depth-Assimilation

The bathymetric file, input in calculations in Sub-section 3.1, is additional information that XMFit does not require to produce output. In this sub-section XMFit simultaneously estimates depths and currents within pre-defined intervals of 0.2 to 30 m and 0 to 2.5 m/s. This does not increase computational cost significantly. The previously observed northwestern bias is stronger and "correct" estimation of southward ADCP velocities by radar is similarly unsuccessful, apart from the experiment's beginning (Figure 6; epochs 1-6). The radar is now susceptible to random error over the whole duration of the experiment, which is attributed to the larger uncertainty in estimating two parameters instead of one.

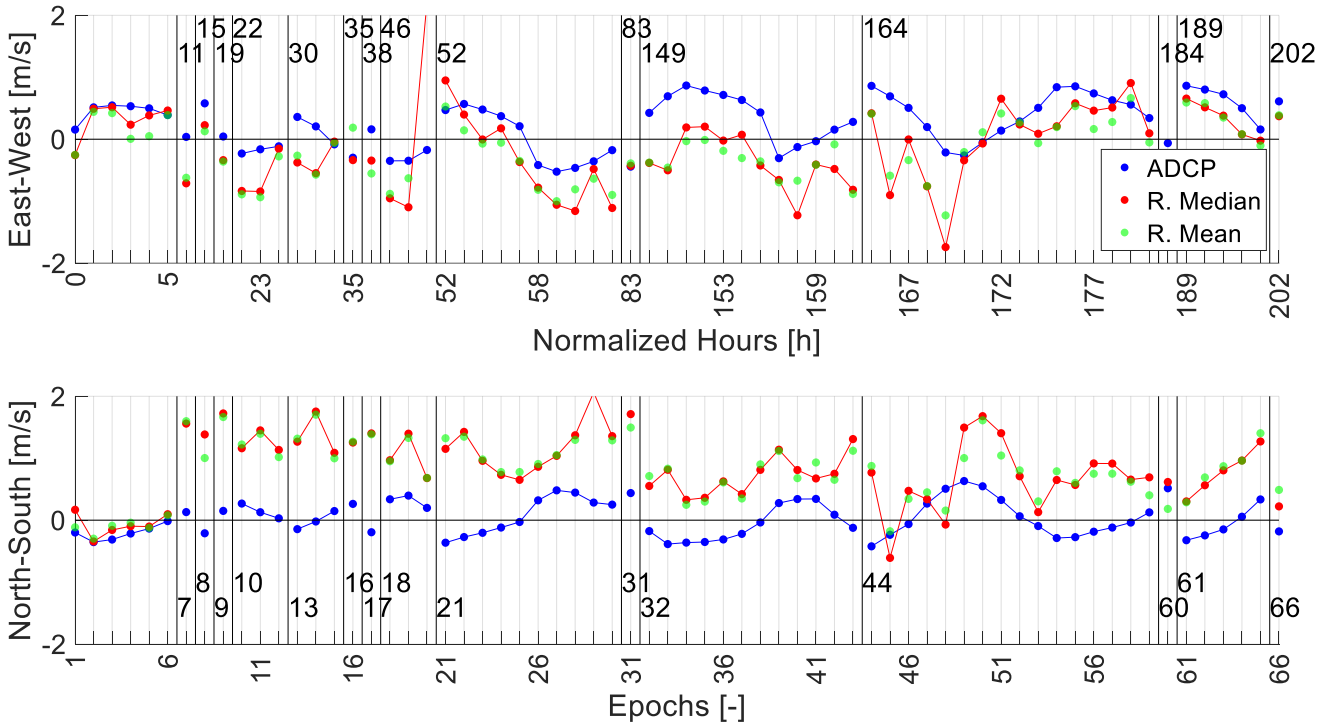

Figure 6 ADCP results (blue) in comparison with radar-derived median (red) and mean (green) estimates for the east-west (top) and north-south (bottom) velocity component at spacing 100 (200) m and with non-depth-assimilated solver for experiment 1. Axes and definitions according to Figure 9.

Regarding the clustering of epochs, decreases in good epochs and increases in bad epochs become visible in all experiments (Table 1 and Table 2). Again, the east-west component is better than the north-south component in time interval 1. Contrary to the depth-assimilated calculations, the north-south component is not better than the east-west component in time interval 2, being much more susceptible to bias. In agreement with the depth-assimilated calculations, the north-south component is characterized by a large tendency towards opposite direction epochs in all experiments (once again resulting from failure to indicate southward velocities; not visible in experiment 3 because of very few epochs at times of southward velocity). The share of overshoots is increased and, because of the large bias, they commonly occur in the east-west (north-south) component at times of westward (northward) velocities. Fewer outliers than in the depth-assimilated calculations are visible. This is because the bias is so large that differences between the graphs are rarely small enough for outliers to form. In depth-assimilated calculations, experiment 4 stands out with its low number of epochs with output (Table 1) but without depth-assimilation no output is produced at all. Compared to calculations with depth-assimilation (Table 1), there are less epochs with output (73.33 %, 61.29 %, 89.47 % and 00.00 %; Table 2), indicating that fitting was less successful.

Table 2 Bias, uRMSE and clustered epochs (defined according to Table 1) for non-depth-assimilated calculations at spacing 100 (200) m.

Experiment		Bias [m/s]	uRMSE [-]	Good [%]	Bad [%]	Opposite [%]	Overshoot [%]	Outlier [%] (1 / 2)
Exp. 1 (66 epochs)	EW	-0.393	0.531	15.15	22.73	28.79	19.70	10.61 / 10.61
	NS	0.816	0.497	04.55	36.36	48.48	31.82	00.00 / 03.03
Exp. 2 (38 epochs)	EW	-0.629	0.395	05.26	31.58	26.32	42.11	13.16 / 10.53
	NS	0.826	0.265	02.63	47.37	44.74	42.11	00.00 / 05.26
Exp. 3 (51 epochs)	EW	-0.564	0.662	09.80	29.41	33.33	19.61	03.92 / 05.88
	NS	1.053	0.571	05.88	58.82	29.41	54.90	00.00 / 05.88
Exp. 4 (00 epochs)	EW	-	-	-	-	-	-	- / -
	NS	-	-	-	-	-	-	- / -

In agreement with depth-assimilated calculations, north-south components are characterized by smaller uRMSE than east-west components (Table 1 and Table 2), stressing the benefits from lower velocity magnitudes and allocation of spectral energy. Surprisingly, all experiments' north-south biases are larger than east-west biases (Table 2). In depth-assimilated calculations, this only applies to the experiments in time interval 1 (Table 1). When assimilating depths, the experiments' biases in east-west and north-south are reduced to respectively 42.24 % / 32.60 %, 70.43 % / 18.28 % and 7.27 % / 17.66 % and the experiments' uRMSEs are changed to respectively 57.25 % / 48.09 %, 119.75 % / 65.66 % and 91.84 % / 73.03 %. Bias is observed to be more affected by depth-assimilation than uRMSE. This is surprising, as the solution is not constrained anymore (without depth-assimilation), allowing substantial fluctuations of depth and current estimates in order to find the best-fitting dispersion shell. However, application of the median over multiple calculation points effectively caters for outlying estimates so that the larger uncertainty from estimating two parameters shows more significantly in the general trend (bias).

There is an improvement in northward bias when comparing experiment 2 to experiment 1 in depth-assimilated calculations but not in calculations without depth-assimilation. When observing the ratio of northward to southward velocities it becomes visible that southward epochs dominate in experiment 1 and northward epochs in experiment 2. In the calculations without depth-assimilation, the southward dominance (in experiment 1) is slightly stronger and the northward dominance (in experiment 2) slightly weaker. Therefore, experiments 1 and 2 feature relatively more southward epochs, which tend to have larger bias than northward epochs (Figure 6 and Figure 9), increasing north-south component bias in the calculations without depth-assimilation. Note, therefore, that bias tends to be larger in the calculations without depth-assimilation partly due to output generation in specific phases of the tidal cycle. Nevertheless, this only causes the substantial bias increase partially.

Epochs in the beginning of experiment 1 are observed to be less susceptible to bias and opposing directions in the north-south component than the rest of the experiment (Figure 6; epochs 1-6). This is surprising, as they entail southward velocities. Observing the corresponding spatial coherence, error metrics and environmental conditions, shows that the conditions are generally favorable for radar imagery. Yet, there is nothing unique to the mentioned epochs that would explain the uniqueness of their bias and southward velocity estimation.

3.3 Ensemble-Averaging at Different Spacings

In the previous analyses, calculation points were spaced in steps of 100 m so that the furthest east-west and north-south distances from the ADCP frames were 200 m (black circles in Figure 2 and Figure 3). The choice of spacing is a balance between incorporating additional areas (every calculation point considers the 0.92 km^2 surrounding it, Figure 3) and deviating the focus of radar calculations from the ADCP location. Ensemble-averaging via spacing of calculation points requires the underlying assumption that the true in-situ velocity applies in all areas considered. The calculation points differ, however, in regard to water depths (either input or solved by XMFit) and spectral information from radar images. Note that larger spacings have the same computational cost as small spacings. To assess the spacing's influence, additional depth-assimilated radar calculations with various spacings (refer to Figure 3 for the relation of two spacings) are conducted.

Table 3 Agreement between ADCP and radar in depth-assimilated calculations for experiment 1 at selected spacings (only the distance between the frame and the first row of calculation points is given in the table). The average number of output points is averaged over all epochs. It decreases at larger spacings because some calculation points are located outside the radar domain (e.g. spacing 500 (1000) m in Figure 2).

Metrics	No Sp.	50 m	100 m	200 m	500 m	600 m	800 m	1250 m	1500 m
Bias Median EW	-0.197	-0.132	-0.166	-0.122	-0.117	-0.081	-0.101	-0.124	-0.121
Bias Median NS	0.275	0.293	0.266	0.222	0.156	0.161	0.191	0.123	0.150
uRMSE Median EW	0.595	0.376	0.304	0.194	0.175	0.120	0.234	0.208	0.231
uRMSE Median NS	0.418	0.256	0.239	0.234	0.211	0.199	0.227	0.120	0.225
Epochs with Output	72	82	90	97	105	104	101	100	91
Av. No. of Output Points	23.3	19.16	16.41	16.42	14.70	13.65	10.88	10.28	9.22
Good Epochs EW/NS [%]	15 / 15	27 / 17	27 / 16	35 / 16	34 / 26	37 / 26	37 / 24	35 / 26	21 / 33
Bad Epochs EW/NS [%]	14 / 4	9 / 4	3 / 7	3 / 3	1 / 2	0 / 1	2 / 3	3 / 0	1 / 2
Opposite Ep. EW/NS [%]	26 / 50	18 / 50	18 / 41	13 / 41	11 / 37	17 / 35	12 / 34	14 / 29	13 / 25

Larger spacings are observed to benefit bias and uRMSE considerably when coming from small spacings to middle-sized spacings of 500 (1000) m or 600 (1200) m (Table 3). At further spacing increase, correlation gets worse again. A similar development is visible for the number of epochs with output, the good and the bad epochs, which are at their best in the middle-sized spacings. Note that in the east-west component, the opposite direction epochs reach a minimum at 500 (1000) m. In the north-south component, however, they keep improving. For further analyses, the spacing 500 (1000) m is chosen.

In comparison to calculations at smaller spacing (Figure 9), bias and random error are substantially reduced (Figure 7). Nevertheless, the first half of experiment 1 is once again observed to be more susceptible to random error than the second half. Even though smaller differences in northward velocities become visible, southward velocities are still not estimated “correctly”.

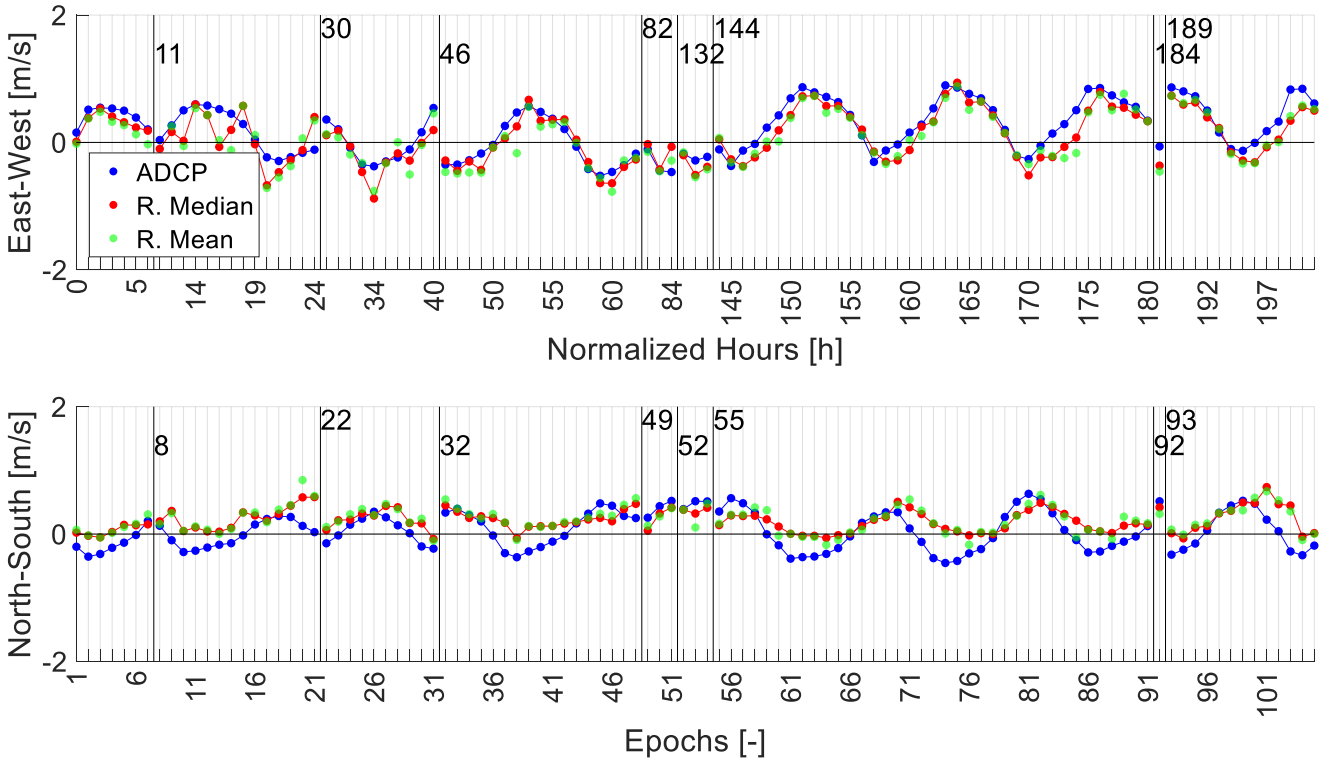

Figure 7 ADCP results (blue) in comparison with radar-derived median (red) and mean (green) estimates for the east-west (top) and north-south (bottom) velocity component at spacing 500 (1000) m and with depth-assimilated solver for experiment 1. Axes and definitions according to Figure 9.

Regarding the clustering of epochs, substantial increases in good epochs and decreases in bad epochs become visible in most components (Table 1 and Table 4). In accordance with calculations at smaller spacing, the east-west component is only better than the north-south component in time interval 1. Once again, the north-south component’s larger tendency towards opposite direction epochs becomes visible. With the bias reduction, the number of overshoots is decreased. This time, the outliers are decreased

because the differences between the graphs and the susceptibility to random error are very small. Compared to depth-assimilated calculations at smaller spacing (Table 1), there are more epochs with output (116.67 %, 124.19 %, 180.70 % and 152.00 %, Table 4).

Table 4 Bias, uRMSE and clustered epochs (defined acc. to Table 1) for depth-assimilated calculations at spacing 500 (1000) m.

Experiment		Bias [m/s]	uRMSE [-]	Good [%]	Bad [%]	Opposite [%]	Overshoot [%]	Outlier [%] (1 / 2)
Exp. 1 (105 epochs)	EW	-0.117	0.175	34.29	00.95	11.43	05.71	05.71 / 01.90
	NS	0.156	0.211	25.71	01.90	37.14	06.67	00.95 / 05.71
Exp. 2 (77 epochs)	EW	-0.215	0.236	25.97	02.60	12.99	14.29	09.09 / 09.09
	NS	0.109	0.165	31.17	00.00	46.75	02.60	01.30 / 00.00
Exp. 3 (103 epochs)	EW	-0.065	0.293	35.92	02.91	08.73	14.56	07.77 / 02.91
	NS	0.093	0.164	48.54	01.94	26.21	06.80	04.85 / 00.97
Exp. 4 (38 epochs)	EW	-0.176	0.374	28.95	13.16	13.16	10.53	13.16 / 13.16
	NS	0.027	0.115	50.00	00.00	28.95	07.89	02.63 / 00.00

In accordance with calculations at smaller spacing (whether depth-assimilated or not), east-west components are characterized by larger uRMSE than north-south components (apart from experiment 1). This stresses, once more, the importance of current magnitudes and allocation of spectral energy for accurate fitting. In agreement with depth-assimilated calculations at smaller spacing, north-south biases are only larger than east-west biases in time interval 1. In accordance with calculations without depth-assimilation (Table 2) and contrary to calculations with depth-assimilation at small spacing (Table 1), experiment 3's bias in the east-west component is westward (Table 4). When increasing the small spacing in depth-assimilated calculations of experiment 3 from 100 (200) m to 150 (300) m, 50 additional epochs with a mainly westward bias become available, causing the bias's change of direction (Table 1 and Table 4). In depth-assimilated calculations at larger spacing, the experiments' biases in east-west and north-south are changed to respectively 70.48 % / 58.65 %, 48.53 % / 72.19 %, -158.54 % / 50.00 % and 21.39 % / 30.34 % and the experiments' uRMSEs are changed to respectively 57.57 % / 88.28 %, 49.89 % / 94.83 %, 48.19 % / 39.33 % and 68.25 % / 50.88 %. Bias and uRMSE are similarly affected by the larger spacing.

Note, furthermore, that the benefit from larger spacing is independent of depth-assimilation. When comparing calculations without depth-assimilation at larger spacing to small spacing, the experiments' biases in east-west and north-south are changed to respectively 83.97 % / 72.30 %, 42.77 % / 49.15 % and 63.12 % / 55.27 % and the experiments' uRMSEs are changed to respectively 48.40 % / 82.49 %, 45.82 % / 69.06 % and 42.15 % / 70.40 %. Furthermore, output for experiment 4 becomes available in 22 epochs. In the other experiments, calculations without depth-assimilation at larger spacing lead to respectively 130.38 %, 152.63 % and 176.47 % of the epochs with output at smaller spacing.

3.4 Environmental Conditions, Error Metrics and Spatial Coherence

No correlation between R^2 or RMSE of the fitting procedure and differences between ADCP and radar is identified in any of the experiments (Figure 8). However, XMFit already uses R^2 and RMSE to filter unreliable outputs. The filtering is observed to cater for the worst outliers. Yet, the predictive capacity of R^2 and RMSE culminates in filtering and does not show potential for further improvements of correlation between ADCP and radar.

Tide gauge measured and ADCP pressure calculated water levels conform to the expected mean water level of 6.5 m with fluctuations of 1-2 m (Figure 11). Velocity leads water level by 2-3 h (Figure 9 and Figure 11), a phase shift the radar captures well. In the north-south component, however, it often fails to capture the change of direction towards the south and mimics it via a decrease in northward velocity magnitude instead (e.g. Figure 9 and Figure 11; epochs 8-11 and 71-76). Here, correlation between ADCP and radar is better during falling tide whereas in the east-west component it is better during rising tide.

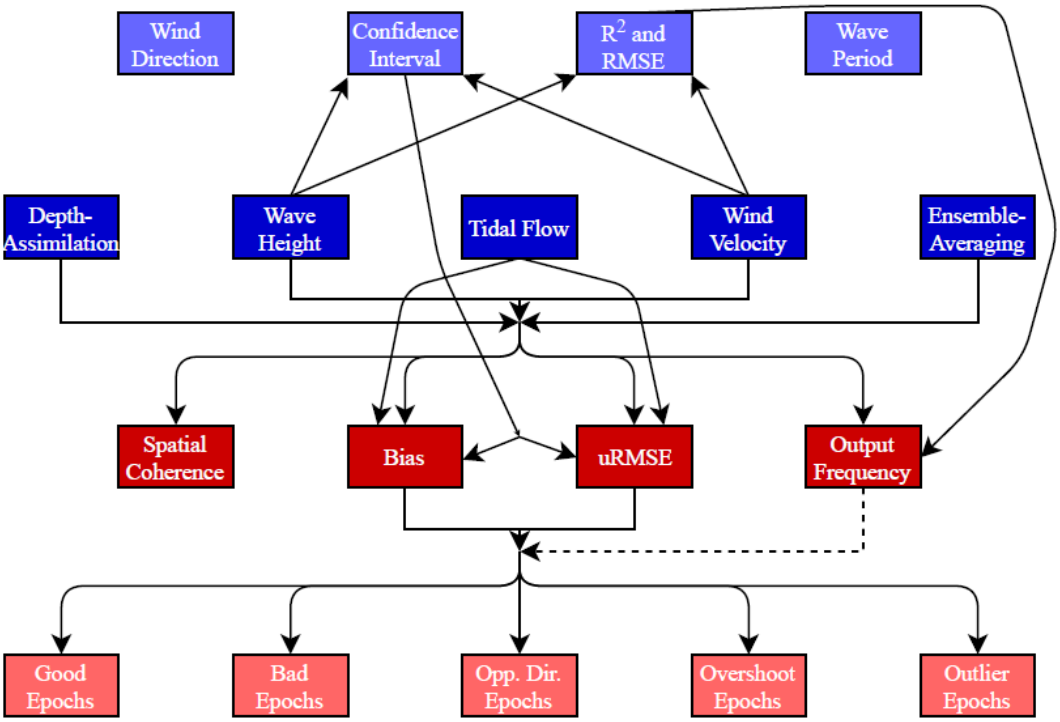

Figure 8 Relations between difference characteristics (dark red), the environmental conditions and calculation settings that influence them (dark blue), the epoch clusters that are influenced by them (light red) and conditions with only secondary influence on difference characteristics (light blue).

In all experiments, no correlation between wave periods T_{m10} and differences between ADCP and radar is found. Note, however, that periods only fluctuate in a limited range (Table 5). As aliasing effects are to be expected in the present frequency range, XMFit's performance under the observed periods is a proof of its anti-aliasing algorithms. Most of experiment 1's first half (Figure 9; epochs 14-47), previously observed to show worse correlation due to increased random error and bias, is characterized by lower wave height than the second half (Figure 10). XMFit requires wave crests to be distinguishable from troughs and at higher waves, shadowing from wave crests benefits the quality of radar images (Nieto Borge et al., 2004). Experience suggests that a significant wave height larger than 0.55 m is needed. The production of output at wave heights well below 0.55 m, however, is a proof of XMFit's robustness. Generally, larger waves are observed to benefit the correlation between radar and ADCP velocities by decreasing differences and outlier frequency (confirmed in experiment 3). Yet, the benefit from higher waves only becomes visible above a certain margin as the wave height fluctuations in experiments 2 and 4 are not large enough for a clear correlation with differences between ADCP and radar.

As expected from the natural relation of wind magnitudes and wave heights, random error- and bias-susceptible epochs in experiment 1 are also characterized by low wind magnitudes (Figure 13). Again, the relation between environmental condition and differences between ADCP and radar is confirmed in experiment 3 whereas wind magnitude fluctuations are not large enough for a clear correlation in experiments 2 and 4 (Table 5). XMFit requires wind for generation of the surface ripples that make backscattering of radar signals possible. Note that larger waves and higher wind velocities do not guarantee small differences between ADCP and radar – they rather have the tendency to coincide with smaller differences and a smaller frequency of outliers. Even though the benefits in north-south correlation from increases in wind magnitude are not clearly visible in experiment 1, they are visible in the corresponding experiment at frame 4 (experiment 3). Furthermore, there are slight indications (most notably in experiment 2) that alignment of wind and current directions benefits the agreement between ADCP and radar.

Table 5 Triangular parameter distributions given as minimum, average per experiment (in parentheses) and maximum. Spatial coherence extracted as difference of 25th and 75th percentiles. Wind given in absolute values. Note that experiments 1 and 3 as well as 2 and 4 were conducted in the same time intervals but radar output has occurred in different epochs during those time intervals, causing alternating values for wave height, period and wind.

Experiment	**Spatial Coherence [m/s] (EW / NS)**	**R^2 / RMSE**	**Confidence Intervals (EW / NS)**	**Wave Height [m] / Period [s]**	**Wind [m/s] (EW / NS / Mag.)**
Exp. 1 (90 ep.)	0.12 (0.78) 2.51 / 0.10 (0.45) 1.83	0.575 (0.820) 0.985 / 0.019 (0.027) 0.046	0.27 (2.39) 8.21/ 0.20 (1.15) 2.88	0.56 (1.07) 1.76 / 3.40 (4.23) 4.95	0.06 (4.74) 11.09 / 0.06 (2.87) 8.10 / 0.39 (5.86) 12.07
Exp. 2 (62 ep.)	0.21 (1.04) 2.52 / 0.03 (0.12) 0.38	0.615 (0.851) 0.964 / 0.022 (0.026) 0.034	1.15 (2.70) 5.35 / 0.16 (0.31) 0.66	0.39 (0.63) 0.78 / 2.89 (3.28) 3.68	0.83 (4.83) 7.58 / 0.12 (1.65) 3.95 / 0.84 (5.23) 7.59
Exp. 3 (57 ep.)	0.05 (0.69) 2.82 / 0.02 (0.62) 2.12	0.463 (0.774) 0.986 / 0.022 (0.034) 0.089	0.27 (1.34) 5.45 / 0.20 (1.25) 4.24	0.56 (1.18) 1.80 / 3.40 (4.14) 4.90	0.44 (6.30) 11.55 / 0.09 (3.26) 8.76 / 0.46 (7.30) 12.45
Exp. 4 (25 ep.)	0.45 (1.18) 2.84 / 0.07 (0.52) 1.50	0.553 (0.814) 0.940 / 0.025 (0.031) 0.044	1.22 (2.80) 6.72 / 0.33 (0.94) 3.59	0.39 (0.53) 0.73 / 2.91 (3.07) 3.56	0.83 (3.78) 7.58 / 0.12 (1.26) 3.87 / 0.84 (4.09) 7.59

The random error- and bias-susceptible epochs also coincide with larger east-west confidence intervals of the fitting procedure (Figure 12; epochs 14-47). With the increase in wave heights and wind magnitudes in the second half of experiment 1 (Figure 12; epochs 48-90), east-west confidence intervals decrease considerably. This indicates that favorable environmental conditions allow more unique fitting, resulting in less outliers and smaller differences between ADCP and radar (not in every single epoch but generally). In both components of experiment 3, smaller wave heights and lower wind magnitudes similarly coincide with the largest confidence intervals, which mark random error- and bias-susceptible epochs. In experiments 2 and 4, where fluctuations in wave heights and wind magnitudes are only small, no coherent relation is detected.

There is a tendency towards better spatial coherence (narrower distribution of velocities in calculation points) at times of high waves and wind magnitudes (Figure 14). Furthermore, spatial coherence is worse in the east-west component (Table 5), which is also more susceptible to bias and random error (Table 1). Therefore, spatial coherence complements previous indications on bias- and random error-susceptibility. Again, the identified relations are only confirmed in experiment 3, as fluctuations in wave heights and wind magnitudes in experiments 2 and 4 are only small. Note that spatial coherence and error metrics are inherent to the radar method. Thus, they are always available and could serve as proxies for environmental conditions in absence of environmental measurements.

One of the striking error sources, the periods of large susceptibility to random error (Figure 9; epochs 14-47), is clearly related to wave heights and wind magnitudes as well as phases in the tidal cycle (falling and rising tide). Correlations with the differences between ADCP and radar are observed even though identification of one-to-one relations (e.g. an epoch of large wave height automatically guarantees small differences between ADCP and radar) proves difficult. The other striking error source, northwestern bias leading to bad correlation between ADCP and radar (especially in the north-south component), remains unclarified and will be investigated in the discussion.

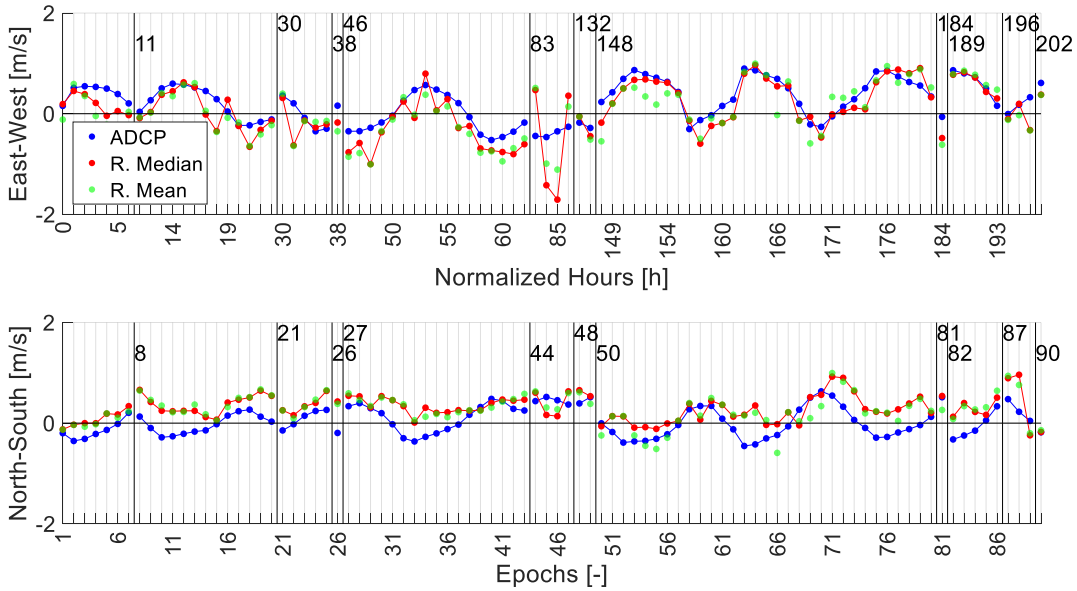

Figure 9 ADCP results (blue) in comparison with radar-derived median (red) and mean (green) estimates for the east-west (top) and north-south (bottom) velocity component at spacing 100 (200) m and with depth-assimilated solver for experiment 1. Flow to the east and north is defined positive and to the west and south is defined negative. On the lower x-axis, epochs are shown in consecutive order up to data gaps (whose number is marked in the upper part of the plot), resulting from quality control measures in radar and in-situ data processing as explained in Section 2. The upper x-axis features the duration of the experiment in hours, normalized to the first epoch 31-Aug-2017 09:32:38 and capturing the size of the data gaps. Here the first normalized hour after the data gaps is marked.

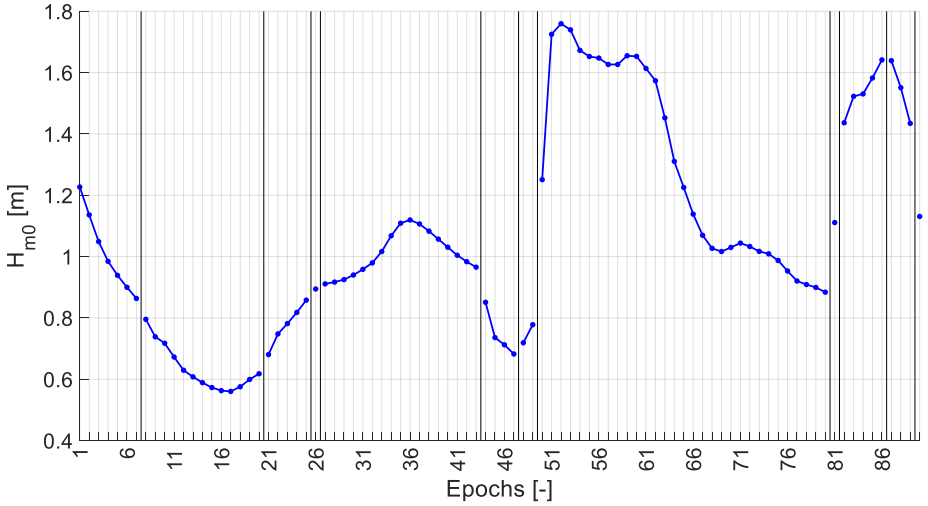

Figure 10 Wave height H_{m0} with definitions and settings corresponding to Figure 9.

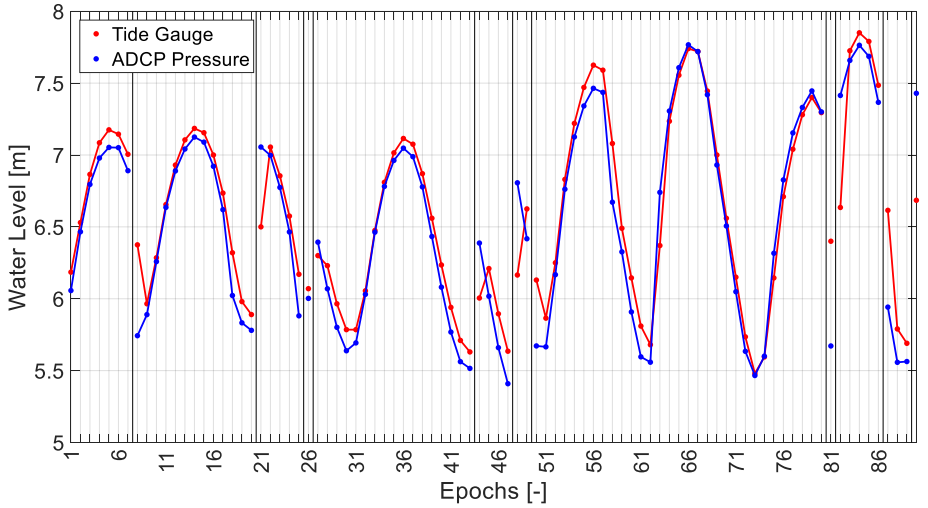

Figure 11 Water levels from tide gauge measurements (red) and pressure measurements (blue) at ADCP frame 1. Definitions and settings corresponding to Figure 9.

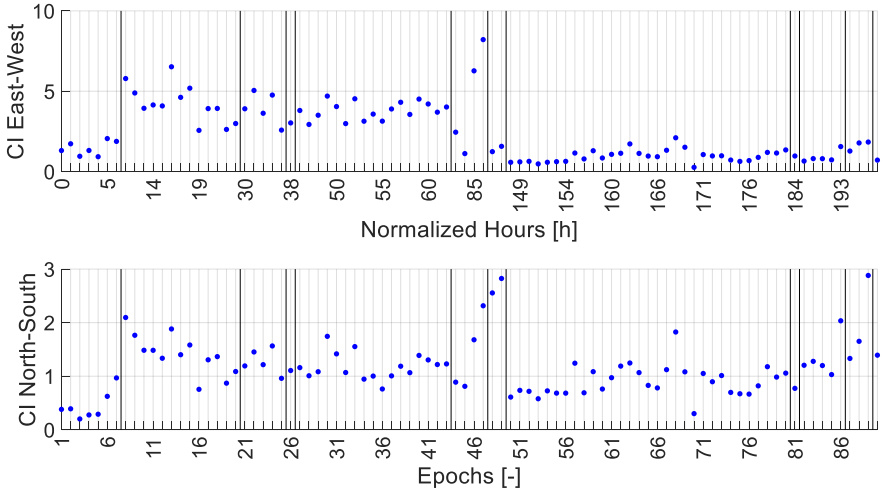

Figure 12 Confidence intervals in east-west (top) and north-south (bottom). Definitions and settings corresponding to Figure 9.

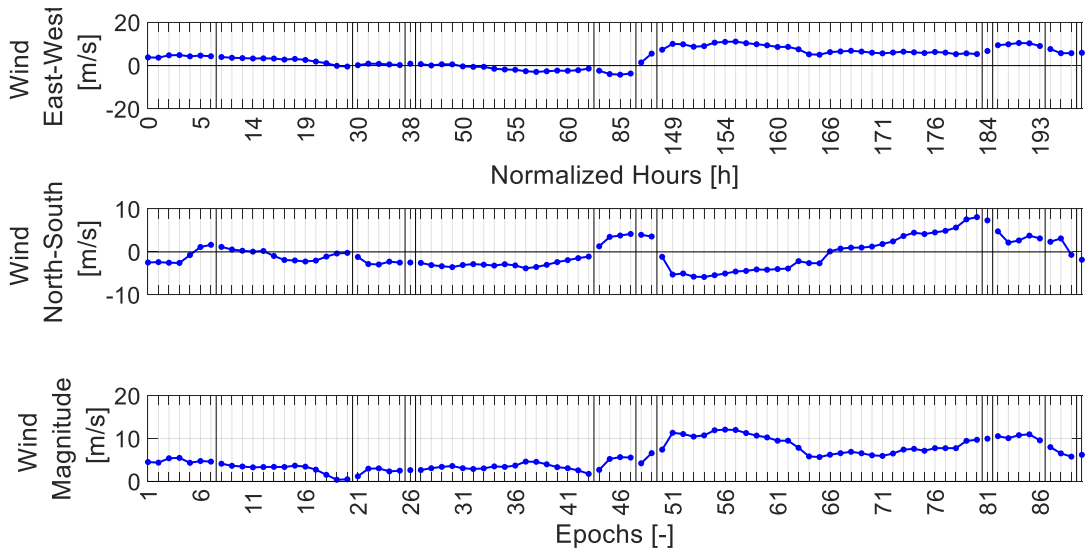

Figure 13 Wind velocity east-west (top), north-south (middle) and magnitude (bottom). Note the changing limits of the y-axes. Definitions and settings corresponding to Figure 9.

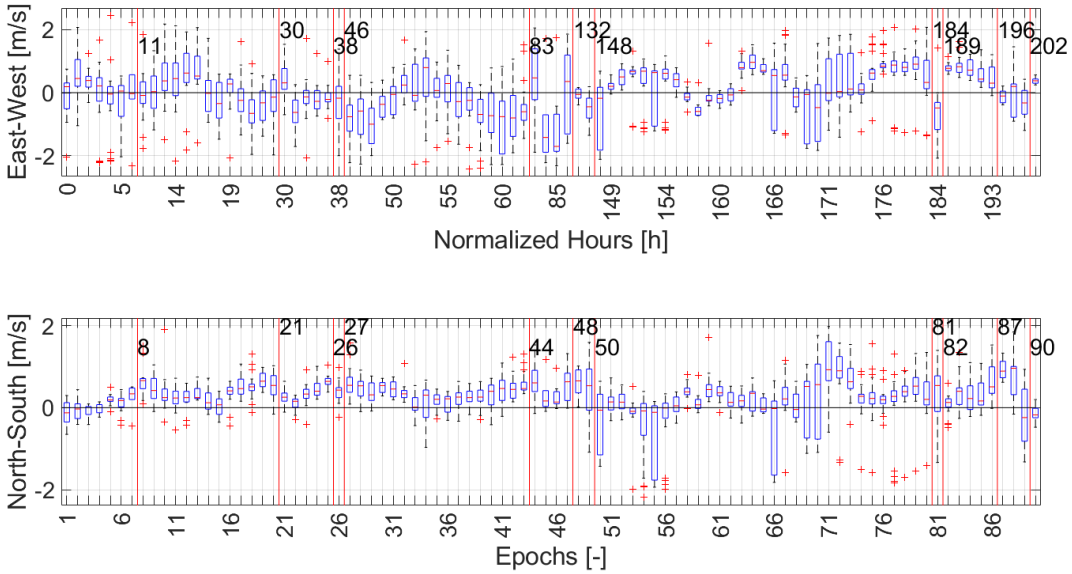

Figure 14 Boxplot of east-west (top) and north-south (bottom) velocity components per epoch. Red horizontal line indicating median per epoch and boxes the 25th and 75th percentiles. Outliers represented by '+' symbol and defined as more than three scaled median absolute deviations. Whiskers representing the most extreme outputs not considered outliers. X-axes corresponding to Figure 9. Good spatial coherence indicated by small boxes and small whiskers. Definitions and settings corresponding to Figure 9.

4 Discussion

The obtained results are reflected and judged in regard to scientific literature, their theoretical background and general applicability. Potential origins of the correlation benefits coinciding with larger spacing of calculation points and potential causes for the unresolved northwestern bias are discussed. Furthermore, applicability of radar to satisfy general monitoring needs and further improvements via filtering based on confidence intervals are tested.

4.1 Spacing of Calculation Points for Ensemble-Averaging

It became visible (Sub-section 3.3) that ensemble-averaging with larger spacing of calculation points has the potential to benefit correlation between ADCP and radar (especially smoothing out random errors) and to increase the frequency of output. Even at very large spacing, correlation is still better than at very small spacing (Table 3). This is surprising, as calculation points at large spacing are located very far from the ADCP position (up to 3 km) and it is unlikely that velocities in a hydrodynamically complex region like Ameland inlet are constant over such a long distance. Furthermore, it is unclear how larger spacing improves correlation – in previous applications XMFit calculation points were usually spaced in steps of 100 m. Therefore, the theoretical background of ensemble-averaging via spacing is discussed in context with the observed relations at spacing variation.

Larger spacing leads to better spatial coherence (e.g. Figure 14 compared to Figure E - 1) and decrease of the average number of calculation points (Table 3). This might result from the influence of local unfavorable conditions on radar current estimation (Figure 3; blue rectangle). Regarding the better spatial coherence, local unfavorable conditions would influence the distribution of velocities more strongly at small spacing (Figure 3; at small spacing, eight calculation points located in unfavorable area but only one calculation point at large spacing). At larger spacing, outliers resulting from local unfavorable conditions are thought to be identified as outliers more easily, not affecting the median over all calculation points (which is the final radar output) as strongly. Regarding the decreasing average number of calculation points, again the relation of radar estimation conditions to the distance between calculation points is thought to be decisive (Figure 3; blue rectangle). At small spacings, when radar estimation conditions are favorable for output in a certain epoch at a certain calculation point, the other calculation points, being located in the calculation point's close vicinity, are likely to have favorable conditions as well. At large spacings, it is not as likely that all calculation points have favorable conditions at the same time, because they are located further from each other. The relation also explains larger spacings' tendency to generate more epochs with output. As the calculation points are located much further from one another, it is more likely that environmental conditions are favorable in at least a few of them. Note that a decrease of the average number of calculation points with outputs at spacings above 300 (600) m (Table 3) occurs because single calculation points are located outside the radar domain (Figure 2).

Furthermore, larger spacing leads to a weighted consideration of additional areas (Figure 3; overlapping orange and magenta squares and Figure 15). Every calculation point utilizes the 0.92 km^2 square around it to calculate a velocity representative of the considered area. By using 25 calculation points, 25 representative velocities are calculated. Via the median, one representative velocity is selected. Indirectly, the areas from all calculation points were used in conjunction (representing 1.85 km^2 at spacing 100 (200) m) to select one velocity (representing 0.92 km^2). Selection via the median ensures that a velocity far from the extremes is chosen. Every additional area adds information to the analysis, which is then assessed in context with previous information. The areas closest to the frames, however, are weighted more heavily than the areas at the borders because they are incorporated in more of the 25 calculation points and to a larger share (Figure 15), as long as averaging areas are close enough to overlap.

Benefits from larger spacing are observed to decrease from 500 (1000) m / 600 (1200) m onwards (Table 3), which is thought to result from two factors. On the one hand, the distance between the calculation points gets so large that the overlapping areas, and thus the relative weighting given to the ADCP location, decrease (Figure 3). This is because the size of the averaging area stays constant while spacing between the calculation points (at which the averaging areas are centered) increases. On the other hand, calculation points are, at large spacing, located far from the ADCP location (Figure 2) with different bathymetry and, potentially, different flow conditions. Nevertheless, the decrease in benefits

at very large spacings is not as substantial as would have been expected and correlation is still better at very large spacings than at very small ones, which is surprising (Table 3). Note that even at very large spacings, most of the calculation points are located on the ETD. This is because calculation points are spread equally in all directions and the radar's range cuts off the points that would have been located outside the ETD region. Apart from deeper sections of the ebb chutes, flow velocities at different phases of the tidal cycle are likely to be similar across the ETD (Elias, 2017 and comparison of depth-averaged velocities from ADCP frames 1 and 4). Furthermore, the ADCP frames are placed in locations that are thought to represent the general flow conditions on the ETD well. This could explain why the correlation between ADCP and radar is good even at very large spacings. However, southward depth-averaged velocities are suspected to occur all across the ETD at times (Elias, 2017) and the radar fails to indicate southward velocities (Figure 6, Figure 7 and Figure 9) very often. At larger spacings, the estimation of southward velocities via radar is more successful but still very much biased towards northward velocities. This indicates that the problem of estimating southward velocities has a partly general and a partly local character.

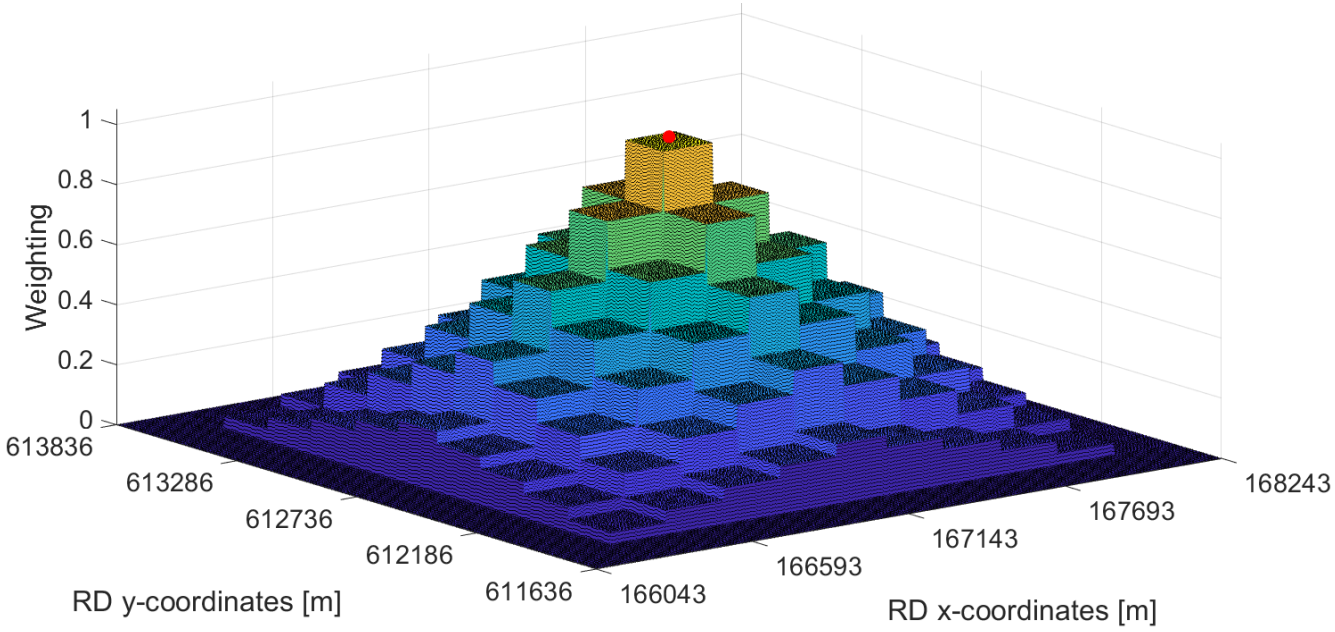

Figure 15 Weighting of averaging areas at spacing 200 (400) m. The respective averaging areas of all calculation points (visible exemplarily for four points as orange and magenta squares in Figure 3) were weighted with 1, then summarized and normalized to the area with largest weighting - at the ADCP location (which is the center of the calculation point grid, marked in red).

Regarding the general character, the median over all calculation points is an important factor in the suppression of southward velocity output. Certain distributions of velocities (Figure 14) contain southward velocities at times of southward ADCP velocities. However, they are often dominated by northward and close-to-zero velocities so that the median is not southward. When observing the location of the southward and northward velocities in the grid of calculation points (Figure 2, black circles), a clear spatial pattern becomes visible. In the northwestern corner and on the western edge of the grid, the indication of southward velocities is "successful". The other calculation points, however, are dominated by northward velocities. In the correctly-indicated southward velocities in calculations without depth-assimilation (Figure 6; epochs 1-6) there is no dominance of northward velocities in the calculation points. Furthermore, calculations without ensemble-averaging and median show that the radar readily estimates southward currents in different parts of the inlet (Figure 17). Of course, it is possible that the "incorrect" northward velocities result from faulty data processing in radar, potentially from the alignment of currents and waves. But as the spatial pattern is coherent, there may be a local physical process that causes the opposing directions (discussed in more detail in Sub-section 4.2).

Larger spacing of calculation points is suspected to benefit the correlation between ADCP and radar because of the weighted incorporation of additional analysis areas (additional spectral information) and less susceptibility to local unfavorable radar estimation conditions. Nevertheless, larger spacings can only be beneficial if there are no strong horizontal velocity gradients. Applying them for the comparison of ADCP and radar velocities in deep sections of the ebb chutes or the inlet gorge (where ADCP frame 3 from the Kustgenese 2.0 campaign is located) would probably result in much worse correlation.

Furthermore, the large benefits observed from larger spacings in this study might be partly mere coincidence, as only two point locations and two time intervals of roughly 12 days in total were assessed.

In any way, some potential for improving the correlation between ADCP and radar via spacing of calculation points was identified and further research into its general applicability is required. Especially the prospect of multi-stage procedures is promising. When monitoring the whole region (and not only the ADCP frame locations), velocities everywhere in the radar's range (resolution depending on discretization of the output grid) are available. Therefore, a multi-stage procedure, involving multiple spacings, could be applied without additional computational cost. The output at larger spacings could be used to select the calculation points for smaller spacings. Furthermore, the calculation points do not need to be spaced equally in all directions from the location of interest (which was the ADCP frame in the present study). They could be adjusted to local bathymetry or other information on local conditions (e.g. flow patterns).

4.2 Northwestern Bias and Depth-Averaging

In most experiments a combination of westward and northward bias is observed. In westward (northward) bias, the radar indicates westward (northward) currents stronger and eastward (southward) currents weaker than indicated by the ADCP – potentially directions are even opposing. The northwestern bias is observed to decrease at larger spacings (Table 3), indicating a local reason for the bias. Use of the median over a grid of calculation points, which is dominated by northward velocities (at times where the ADCP indicates southward currents), was linked to the observed bias (Sub-section 3.2). It remains to assess why there could be a dominance of northward velocities in the calculation points.

The "incorrect" northward velocities are hypothesized to result from the combination of a local flow process and ADCPs' and radar's different consideration of the in-situ velocity profile (Figure 4). As radar measures near-surface currents, it accounts for the top part of the profile the ADCP is missing. Measured ADCP data features deviations from the logarithmic profile shape when approaching the missing top part (e.g. Figure 4). But due to difficulties with ADCP measurements in this part of the profile, the extent of the profile shape deviations is unclear. To explore this possibility, the unknown shape of the profile at the top of the water column is assumed linear (for simplicity). Furthermore, a worst case, where radar only captures the ADCP-ignored profile region and ADCP does not capture the region at all, is assumed (Figure 16). The depth-averages from ADCP and radar are observed to differ significantly and the difference is more striking at times when the unknown profile section increases the overall depth-averaged velocity of the profile. Furthermore, a shallower radar averaging depth is observed to lead to larger differences between the ADCP and radar depth-averages (Figure 16).

Four potential local flow processes, that could lead to the necessary reshaping of the profile, are discussed. First, suspended fine sediments on Ameland's ETD were recently found to originate from within the Wadden Sea (Pearson et al., 2019). This indicates the existence of flows from deep within the Wadden Sea through the inlet and onto the ETD during ebb tide (Pearson et al., 2019). As there is freshwater supply to the Western Wadden Sea via discharge sluices in the Afsluitdijk (Duran-Matute et al., 2014), the fine sediment carrying flows, observed in Ameland Inlet, could also carry freshwater with them. In estuaries, freshwater is commonly known to slide on top of the denser saltwater, leading to vertical gradients in horizontal velocity (Geyer and MacCready, 2014). Both ADCP frames are located at the end of ebb chutes (Figure 2) and local bathymetry could serve as a lift-off point for freshwater plumes (e.g. Kilcher and Nash, 2010), reshaping the velocity profile in near-surface regions. Measurements of vertical salinity profiles in the frames' vicinity are required to ascertain this hypothesis. Note that ebb flows are directed to the northwest, as is bias.

Second, wind is known to influence especially near-surface currents. Teague et al. (2001) found a moderate to high correlation between HF radar current direction and wind velocity and direction. Campana et al. (2017) observed amplification of the near-surface current in the alongwind direction, indicating that their X-band radar current estimates account for wind-induced currents. In this study, however, no correlation between wind direction and bias was observed. Furthermore, bias was observed to decrease at times of higher wind magnitudes (where wind would have a stronger influence on the profile) – yet, it is possible that benefits from higher waves and larger wind velocities for radar analysis outweigh the inaccuracies from wind-induced currents reshaping the profile. In any way, the northwestern bias is observed to operate constantly in most of the epochs. It is unlikely that the freshwater and wind-induced currents are operating constantly over long durations.

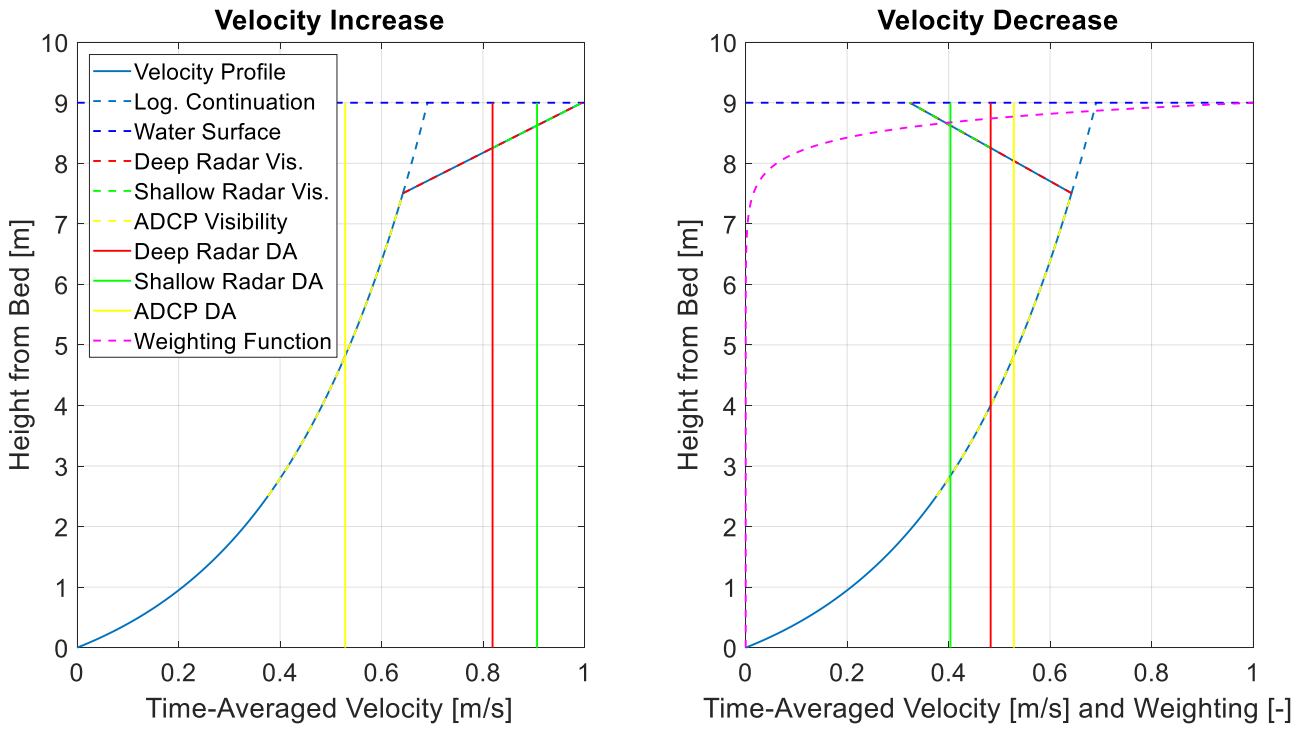

Figure 16 Thought experiment on effects on depth-averaging from profile shape deviations in the ADCP-ignored part of the profile. Deformed velocity profile (light blue) in relation to its logarithmic continuation (light blue dashed) up to the water surface (dark blue). Profile sections considered for deep radar averaging (red dashed), shallow radar averaging (green dashed) and ADCP-averaging (yellow dashed) shown on top of the deformed velocity profile. Resulting depth-averages shown as solid lines. Normalized weighting function (Kirby and Chen, 1989; shown in magenta for T = 4.5 s) indicating the importance of profile depths for effective velocity.

Third, water level gradient-driven currents could be the reason. Both ADCP frames and surrounding radar calculation points are located on the outward slope of the ETD (Figure 2). Calculations for the full radar domain indicate coherent current patterns pointing away from regions of shallower water depth (Figure 17). In contrast to freshwater and wind-induced currents, water level gradient-driven currents could explain the continuous character of northwestern bias. Furthermore, at larger spacings, when less calculation points are located on the outward slope in the direct vicinity of the frames, the problem with southward current estimation is observed to decrease (Table 3). However, it is doubtful if water level gradient-driven currents could reshape the profile in the required way. To ascertain this hypothesis, hydrodynamic modelling under consideration of the bathymetric file used in this study is recommended.

Fourth, due to the present bathymetric gradients (Figure 2), wave-induced currents could occur at the considered locations. Regarding the vertical structure of such currents, the undertow is known to be an important seaward-directed current. However, it acts in the bottom of the water column where the radar is probably not measuring. Nevertheless, due to the uneven distribution of radiation stress in the watercolumn, “A fluid particle below mean trough level will … experience a net force averaged over the wave period which is directed seaward.” (Bosboom and Stive, 2015, p. 215). As the way the effective velocity affects the wave spectrum is not known in much detail, it may be possible that radar’s depth-averaging captures this net force as a current, yielding the observed northwestern bias.

Note that the hypothesis of local flows as the cause of northwestern bias involves many assumptions that may not hold. In-situ radar depth-averaging could incorporate similar parts of the velocity profile as the ADCP, for example. Furthermore, the hypothesized causes of local flows also involve many assumptions that may not hold. The freshwater currents could easily be well-mixed by the time they reach the frames, for example. Apart from a physical cause of the northwestern bias, problems in data processing with radar could be the cause. In addition to freshwater plumes, Tenthof van Noorden (2015) mentions precipitation, applicability of the linear dispersion relation and amplitude dispersion.

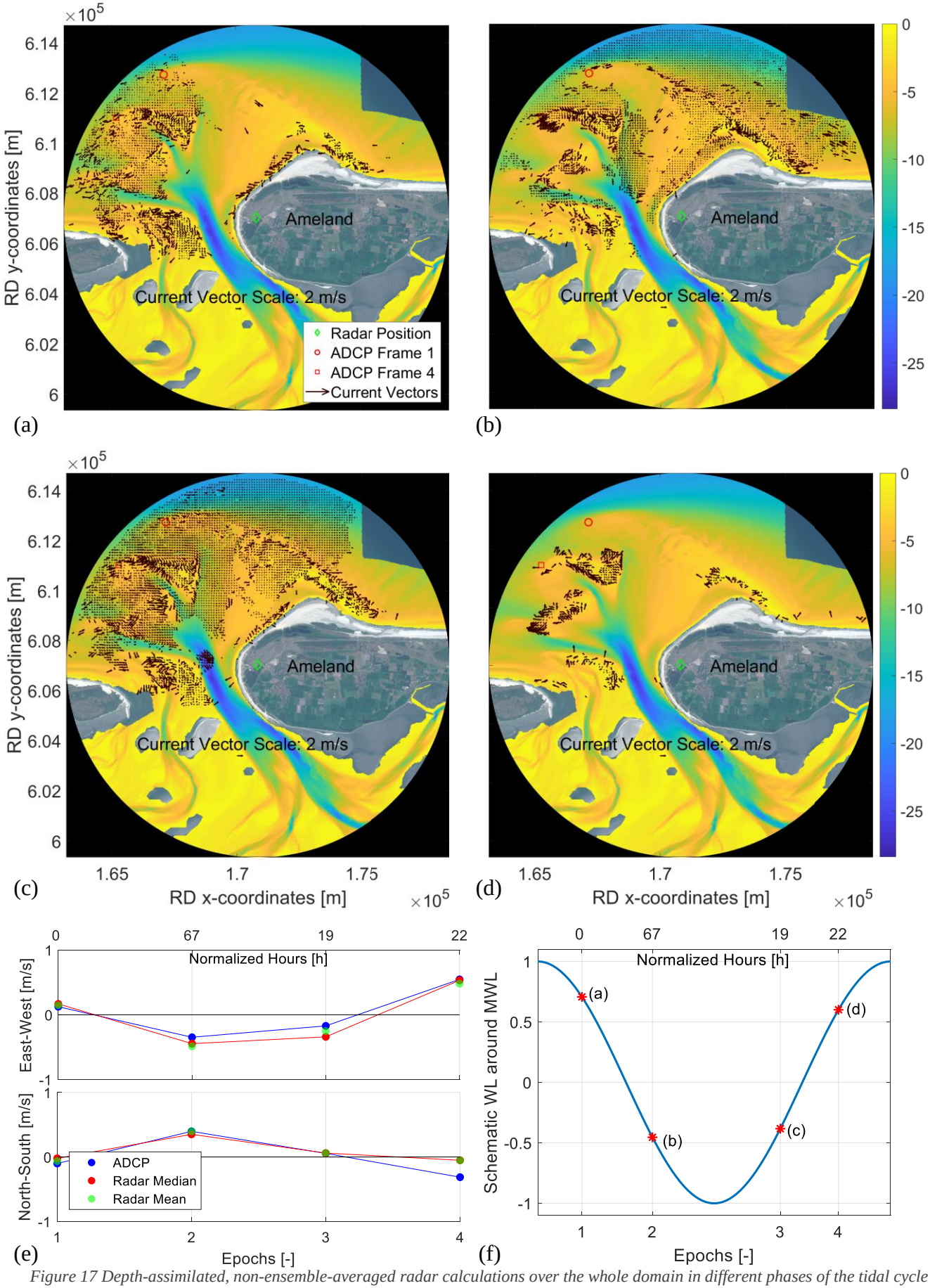

Figure 17 Depth-assimilated, non-ensemble-averaged radar calculations over the whole domain in different phases of the tidal cycle (a-d related as shown in f). Note that the shown epochs are not consecutive and selection was based on small differences between ADCP and radar in depth-assimilated calculations with ensemble-averaging at spacing 500 (1000) m (e, definitions and settings according to Figure 9). The epochs on the upper x-axes are normalized to 30.8.2017 12:32. Currents were only calculated for the inlet and ETD. The colorbars on the right indicate water depths.

4.3 Satisfying Monitoring Needs

At the locations of the frames, generally good agreement becomes visible (Figure 7 and Table 4). Bias and uRMSE are reduced by depth-assimilation and ensemble-averaging so that the share of good epochs is much higher than the share of bad epochs. However, a tendency towards northwestern bias remains and the failure to indicate southward currents is a considerable problem. Keeping this in mind, monitoring of currents at the frame locations would still be possible, as the radar indicates maximum velocities and their directions in good agreement with the ADCP throughout the tidal cycle.

When considering the obtained results in regard to other locations in the tidal inlet system, gradients of bathymetry and velocity play an important role. Large gradients in XMFit's averaging areas (Figure 3) inherently lead to problems, as its 3D-FFT assumes the same wave and current field to apply everywhere in the averaging area. In XMFit bathymetry calculations, a potential link between so-called "Hanning Windows", which reshape the input signal to guarantee a smoother FFT, and the accurate calculation of large bathymetric gradients was identified. Whether this could also apply to currents is uncertain but possible. Nevertheless, especially the channels should be challenging for radar calculations. Furthermore, the present case study was focused on two specific locations. The problems observed with estimation of southward velocities could be of local origin as well as the benefits from ensemble-averaging at larger spacing of calculation points (because the ADCP depth-averages could have coincidentally agreed with the results from averaging radar over the whole ETD).

Therefore, calculations without ensemble-averaging for the outer part of the inlet system are conducted (Figure 17, a-d). The presented epochs were selected due to the small differences between ADCPs and ensemble-averaged radar estimates (Figure 17, e). In the whole system, coherent current patterns, in agreement with expectations, become visible in different phases of the tidal cycle (e.g. Figure 17; a: outflow through the ebb chute leading to frame 4; b: stronger outflow through both ebb chutes and lower current velocities outside the ETD region; c: inflow through the inlet gorge; d: flow diverting from areas of shallower depth). Furthermore, the current velocities and directions generally agree with expectations from a process-based (Delft3D) model (Elias, 2017).

Note, however, that without ensemble-averaging, data availability is reduced and comparison of currents at the frame locations would not have been possible in some of the four shown epochs (Figure 17). Thus, limited data availability could inhibit the applicability of XMFit in coastal monitoring. Nevertheless, even without ensemble-averaging it is possible to use the output of a neighboring calculation point, if no output is produced at the point of interest. Furthermore, the input of a bathymetric file (depth-assimilation) was observed to be very important for bias reduction. In monitoring practice, bathymetric files may not be available or outdated due to the large efforts and costs for obtaining them. This could further limit the applicability of XMFit in coastal monitoring.

Nevertheless, complex current fields cannot be monitored at an appropriate scale with point measurements only (Hessner et al., 2015). Radar provides the opportunity to monitor the whole inlet system and observe the spatial coherence of currents. This can be done at high temporal resolution and low cost. If key issues (data availability, susceptibility to bias and uRMSE and physical understanding of the radar current) can be addressed by future research, there is large potential for radar in coastal monitoring.

4.4 Confidence Interval Filtering

Large confidence intervals of the fitting procedure were observed to coincide with large differences between ADCP and radar (Sub-section 3.4). Thus, there might be potential for output filtering based on confidence intervals. However, two conditions should be fulfilled. First, a large span of confidence intervals, as commonly seen in the east-west component (most notably in experiment 1, Table 5), is required. Only then, confidence intervals can non-arbitrarily be divided into large and small. Second, good environmental conditions are required. Then, confidence intervals are observed to be smaller and the largest ones arise from problematic fitting (which confidence intervals assess).

When filtering, it is crucial to select the right cut-off margins. Many combinations of confidence interval cut-off margins ranging from 2-8.2115 (max) in the east-west component and 1-2.8806 (max) in the north-south are applied. The lowest absolute sum of bias and uRMSE is achieved with margins of 2.0498 in the east-west component and 1.0635 in the north-south component. They change bias in the east-west and north-south components to respectively 80.29 % / 101.09 % and uRMSE to respectively 76.49 % / 82.36 % (when compared to non-filtered calculations, Figure 9). The cut-off margins are very close to the lowest permissible ones. This indicates that epochs with low confidence intervals tend to show better agreement with ADCP results. However, filtering must balance the needs of accuracy and frequency of output. When applying the optimized cut-off margins, only 54.44 % and 45.56 % of the epochs in east-west and north-south remain. Therefore, alternative cut-off margins of 4.5 in the east-west component and 2 in the north-south component are chosen by expert judgement. This leads to smaller benefits in agreement between ADCP and radar (biases changed to respectively 85.28 % / 102.82 % and uRMSEs changed to respectively 85.24 % / 98.87 %) but balances the need for high output frequency more effectively (Figure 18).

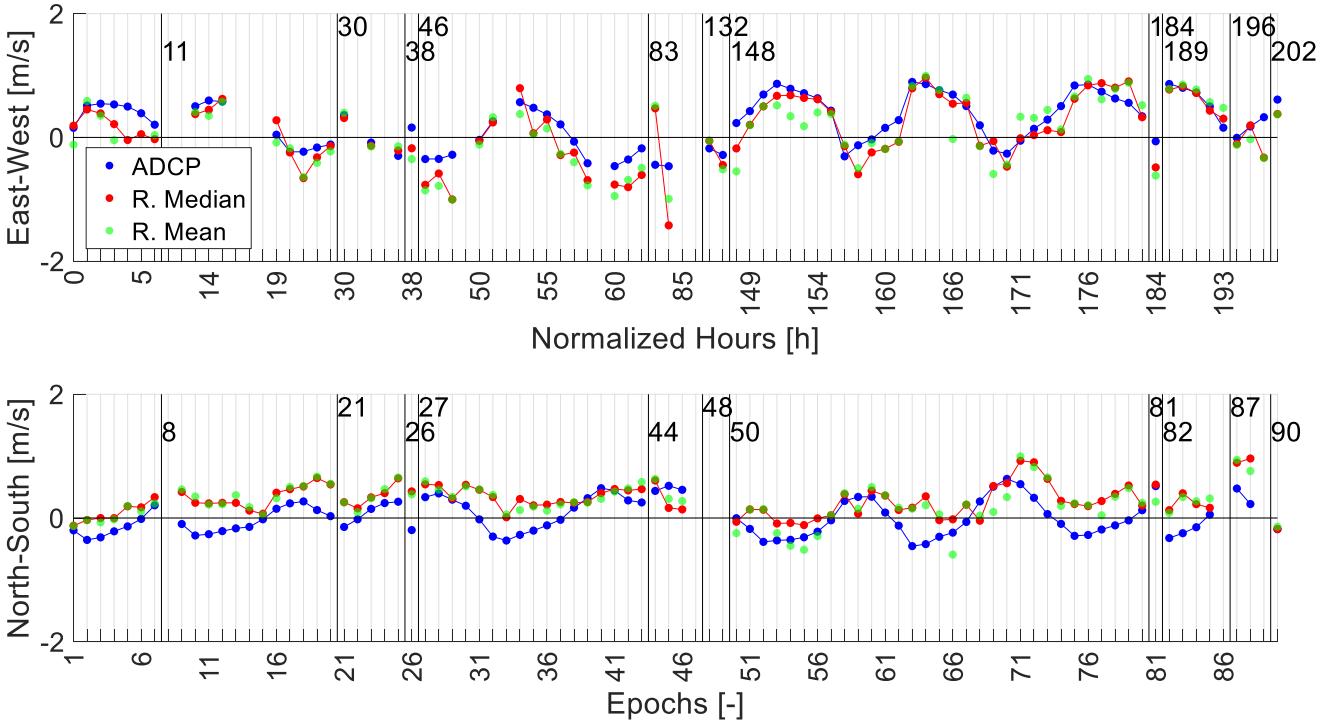

Figure 18 ADCP results (blue) in comparison with confidence interval-filtered radar-derived median (red) and mean (green) estimates for the east-west (top) and north-south (bottom) velocity component at spacing 100 (200) m and with depth-assimilated solver. Axes and definitions according to Figure 9.

5 Conclusions

Remote sensing velocity component estimates from X-band radar were compared to depth-averaged in-situ measurements from Acoustic Doppler Current Profilers (ADCPs) during a field campaign in September 2017 at Ameland inlet. In the east-west and north-south velocity components, good agreement between ADCPs and radar was found with respective bias of -0.143 and 0.096 and respective unbiased Root-Mean-Square-Error (uRMSE) of 0.270 and 0.164 (averaged over the four experiments with depth-assimilation and large calculation point spacing in Sub-section 3.3).

Assimilation of depths (via input of a bathymetric file) and ensemble-averaging (via multiple calculation points in the ADCP frames' vicinity) proved to be very effective in the reduction of bias and uRMSE (quantifying random error) and in the increase of radar output frequency. Nevertheless, this case study highlights radar's striking tendency towards northwestern bias and failure to indicate southward currents. Despite ensemble-averaging's benefits, it was linked to the observed bias and it was shown that its use requires careful considerations (towards the placement of calculation points as well as the interpretation of output). Local profile-reshaping currents and their interplay with the depth-averaging procedures in ADCP and radar were identified as another potential reason for the observed bias, stressing that observed problems may be specific to the comparison locations used. In

the present mean water depth regimes (6.5 and 8.7 m), no correlation between averaging depth in radar (Steward and Joy, 1974) and differences between ADCP and radar could be identified. The environmental conditions wave height, wind magnitude and phase of the tidal cycle, in contrast, correlated with bias and uRMSE. Larger confidence intervals of the radar fitting procedure coincided with larger differences between ADCP and radar and potential for output filtering based on confidence intervals was shown.

The study shows that, with the right calculation settings (depth-assimilation and optimized calculation point spacing according to local conditions) and under favorable radar estimation conditions (wave heights larger than ≈ 1 m, wind velocities larger than ≈ 5 m/s, confidence intervals of the radar fitting method smaller than ≈ 1-2, rising tide in the east-west component and falling tide in the north-south component), radar currents conform to ADCP depth-averaged currents (from 0.48-0.7 m below the water surface to 2.5-3.2 m above the seabed). In combination with its large spatial coverage and the ability to assess spatial coherence of currents, this highlights radar's potential for coastal monitoring applications.

6 Recommendations

For a thorough investigation of depth-averaging in radar and the physical meaning of radar's depth-average, better data quality is required. At the beginning of the research for this study, it was aimed to inversely solve for radar averaging depth, applying and testing equation (1) in-situ. This required an ADCP validation profile ranging from the lower parts of the water column to the water surface. Due to difficulties with near-surface measurements (the profile region that is assumed to be most important for radar, refer to weighting function in Figure 16), this could not be taken into action. In controlled laboratory conditions, velocity profiles are readily available (e.g. Schmeltzer et al., 2019 *in prep*), but accurate in-situ measurements of the velocity profile are not obtained easily. The use of ADCPs with surface tracking has a better chance (than the presently used ADCPs) to yield the required in-situ profile. Furthermore, the ADCPs should be placed closer to the bed to cover an even large portion of the velocity profile. To research radar's depth-averaging, it would be useful to observe a pattern in differences when comparing to conventional depth-averaged currents from in-situ measurements (e.g. there is better agreement during certain phases of the tidal cycle due to surface elevation or velocity profile shapes). To do so, a location with deeper water depth, larger tidal amplitudes and larger velocity profile gradients is recommended. Note, however, that separation of the many error sources, which radar calculations of velocity usually entail, is an ever-complicating factor. Large datasets may help with error source separation.

Regarding future studies for comparing radar and ADCP currents at Ameland inlet, three ideas are discussed. The comparison's focus should shift from individual points to areal considerations, to allow better conclusions on the general applicability of radar in coastal monitoring and the severity of the problems with northwestern bias and indication of southward velocities. Potentially, it is possible to use a numerical model for comparison in many different points (even though numerical models are subject to large inaccuracies themselves and mostly operate in a depth-averaged mode). Furthermore, the present study was limited to less than two weeks whereas the continuous operation of the Ameland radar allows the generation of large datasets. In addition to the environmental conditions observed in this study, other environmental conditions may also show correlations with ADCP and radar (e.g a more holistic description of the present wave spectrum and its wavenumbers).

Regarding further steps that should be conducted with the presently available data, five ideas for improvements are discussed. It was shown that the median over calculation points provides better correlation with ADCP measurements than the mean. Another statistical measure, providing even better correlation than the median and treating southward velocities in the north-south component separately, could be developed. Furthermore, the potential of the previously mentioned multi-stage procedure (Sub-section 4.1) and of reshaping the spatial distribution of calculation points must be assessed. In this context, scale-selective methods could be useful (e.g. Bosboom and Reniers, 2014). Additionally, the sensitivity to many other XMFit calculation settings should be assessed (e.g. the size of the averaging area per output velocity in relation to the spacing of calculation points). Also, ADCP data from another frame, placed in the inlet gorge, is available. As the bathymetry is very different and the mean water depth much larger, this frame may allow to clarify whether the northwestern bias observed in this study resulted from local conditions. Furthermore, it would provide important indications on the generally

applicability of radar in coastal monitoring. In respect to general applicability, it would be important to assess the correlation between single radar estimates and ADCP measurements (as this study focuses on ensemble-averages).

7 References

Bass, F., Fuks, I., Kalmykov, A., Ostrovsky, I., Rosenberg, A., 1968. Very High Frequency Radiowave Scattering by a Disturbed Sea Surface Part I: Scattering from a Slightly Disturbed Boundary. IEEE Transactions on Antennas and Propagation, 16, 554-59.

Bosboom, J., Reniers, A., 2014. SCALE-SELECTIVE VALIDATION OF MORPHODYNAMIC MODELS. Coastal Engineering Proceedings, 34, sediment. 75.

Bosboom, J., Stive, M.J.F., 2015. Coastal Dynamics I, Version 0.5. Delft Academic Press.

Campana, J., Terrill, E.J., Paolo, T., 2016. The Development of an Inversion Technique to Extract Vertical Current Profiles from X-Band Radar Observations. Journal of Atmospheric and Oceanic Technology, 33, 2015-2028.

Campana, J., Terrill, E.J., Paolo, T., 2017. A New Inversion Method to Obtain Upper-Ocean Current-Depth Profiles Using X-Band Observations of Deep-Water Waves. Journal of Atmospheric and Oceanic Technology, 34, 957-970.

Crombie, D. D., 1955. Doppler Spectrum of Sea Echo at 13.56 Mc./S. Nature, 175, 681-82.

Duran-Matute, M., Gerkema, T., de Boer, G.J., Nauw, J.J., Gräwe, U., 2014. Residual circulation and freshwater transport in the DutchWadden Sea: a numerical modelling study. Ocean Science, 10, 611-632.

Elias, E., 2017. Understanding the present-day morphodynamics of Ameland inlet. Deltares Report for Rijkswaterstaat. Reference 1220339-006-ZKS-0006.

Entekhabi, D.; Yueh, S.; O'Neill, P.E.; Kellogg, K.H.; Allen, A.; Bindlish, R.; Brown, M.; Chan, S.; Colliander, A.; Crow, W.T., 2014. SMAP Handbook–Soil Moisture Active Passive: Mapping Soil Moisture and Freeze/Thaw From Space. Jet Propulsion Laboratory: Pasadena, CA, USA.

Friedman, J., 2014. Development of an X-band Radar Depth Inversion Model at the Sand Motor. Master Thesis, Delft University of Technology, Available: https://repository.tudelft.nl/islandora/object/uuid%3A2d4773bd-50e5-4507-ae64-1b7c333fb7c1

Gangeskar, R., 2018. Verifying High-Accuracy Ocean Surface Current Measurements by X-Band Radar for Fixed and Moving Installations. IEEE Transactions on Geoscience and Remote Sensing, 56, 4845-4855.

Gawehn, M., Swinkels, C., van Dongeren, A., Hoekstra, R., de Vries, S., Aarninkhof, S.G.J., 2019. A Radar-based depth inversion method to monitor the evolution of nourishments on complex coasts. In preparation.

Geyer, W.R., MacCready, P., 2014. The Estuarine Circulation. Annual Review of Fluid Mechanics, 46, 175-197.

Ha, E.C., 1979. Remote Sensing of Ocean Surface Current and Current Shear by Hf Backscatter Radar. PhD Thesis, Stanford University, Available: https://apps.dtic.mil/dtic/tr/fulltext/u2/a078834.pdf

Hessner, K., Bell, P.S., 2009. High Resolution Current & Bathymetry Determined by Nautical X-Band Radar in Shallow Waters, in: OCEANS 2009-EUROPE.

Hessner, K., Wallbridge, S., Dolphin, T., 2015. Validation of Areal Wave and Current Measurements Based on X-Band Radar, in: IEEE/OES Eleveth Current, Waves and Turbulence Measurement (CWTM).

Holman, R., Haller, M.C., 2013. Remote Sensing of the Nearshore. Annual Review of Marine Science, 5, 95-113.

Kilcher, L.F., Nash, J.D., 2010. Structure and dynamics of the Columbia River tidal plume front. Journal of Geophysical Research: Oceans, 115, C05S90.

Kirby, J.T., Chen, T.-M., 1989. Surface Waves on Vertically Sheared Flows: Approximate Dispersion Relations. Journal of Geophysical Research: Oceans, 94, 1013-1027.

Lee, P. H. Y., Barter, J. D., Beach, K. L., Hindman, C. L., Lake, B. M., Rungaldier, H., Shelton J. C, Williams, A.B., Yee, R., Yuen, H.C., 1995. X Band Microwave Backscattering from Ocean Waves. Journal of Geophysical Research: Oceans, 100, 2591-2611.

Ludeno, G., Nasello, G., Raffa, F., Ciraolo, G., Soldovieri, F., Serafino, F., 2016. A Comparison between Drifter and X-Band Wave Radar for Sea Surface Current Estimation. Remote Sensing, 8, 621.

Lund, B., Graber, H.C., Hessner, K., Williams, N.J., 2015. On Shipboard Marine X-Band Radar near-Surface Current ‘‘Calibration’’. Journal of Atmospheric and Oceanic Technology, 32, 1928-44.

Mueller, D.S., 2015. Velocity bias induced by flow patterns around ADCPs and associated deployment platforms, in: IEEE/OES Eleveth Current, Waves and Turbulence Measurement (CWTM).

Nieto Borge, J., Rodríguez, G.R., Hessner, K., Gonzáles, P.I., 2004. Inversion of Marine Radar Images for Surface Wave Analysis. Journal of Atmospheric and Oceanic Technology, 21, 1291-1300.

Pearson, S.G., van Prooijen, B.C., de Wit, F.P., Meijer-Holzhauer, H., de Looff, A.P., Wang, Z.B., 2019. Observations of suspended particle size distribution on an energetic ebb-tidal delta, in: Coastal Sediments 2019, 1991-2003.

Plant, W. J., Keller, W.C., 1990. Evidence of Bragg Scattering in Microwave Doppler Spectra of Sea Return. Journal of Geophysical Research: Oceans, 95, 16299-16310.

Schmeltzer, B.K., Æsøy, E., Ådnøy, A., Ellingsen, S. Å., 2019. An improved method for determining near-surface currents from wave dispersion measurements. In preparation.

Senet, C.M., Seeman, J., Ziemer, F., 2001. The near-surface velocity determined from image sequences of the sea surface. IEEE Transactions on Geoscience and Remote Sensing, 39, 492-505.

Senet, C. M., Seemann, J., Flampouris, S., Ziemer, F., 2008. Determination of Bathymetric and Current Maps by the Method Disc Based on the Analysis of Nautical X-Band Radar Image Sequences of the Sea Surface. IEEE Transactions on Geoscience and Remote Sensing, 46, 2267-2279.

Stewart, R.H., Joy, J.W., 1974. HF radio measurements of surface currents. Deep Sea Research and Oceanographic Abstracts, 21, 1039-1049.

Teague, C. C., Vesecky, J. F., Hallock, Z. R, 2001. A Comparison of Multifrequency Hf Radar and Adcp Measurements of near-Surface Currents During Cope-3. IEEE Journal of Oceanic Engineering, 26, 399-405.

Tenthof van Noorden, C., 2015. The Accuracy and Error Sources of Radar-derived Bathymetry by the XMFit Algorithm. Master Thesis, Delft University of Technology,
Available: https://repository.tudelft.nl/islandora/object/uuid%3Aa93514c2-721a-490f-bcda-626dec1d61c8

Terrill, E., Otero, M., Hazard, L., Conlee, D., Harlan, J., Kohut, J., Reuter, P., Cook, T., Harris, T., Lindquist, K., 2006. Data Management and Real-Time Distribution in the Hf-Radar National Network, in: OCEANS 2006.

Trizna, D., Xu, L., 2006. Target Classification and Remote Sensing of Ocean Current Shear Using a Dual-Use Multifrequency Hf Radar. IEEE Journal of Oceanic Engineering 31, 904-918.

Valenzuela, G. R., 1978. Theories for the interaction of electromagnetic and oceanic waves - a review. Boundary-Layer Meteorology, 13, 61-85.

Weijenborg, A. J., 2015. Validation of X-Band Radar-Derived Current Measurements at the Sand Engine. Master Thesis, Delft University of Technology, Available: https://repository.tudelft.nl/islandora/object/uuid%3A9a7bcce1-ccda-4c8c-a977-6f160a3c59fd?collection=education

Wetzel, L.B., 1990. Electromagnetic Scattering from the Sea at Low Grazing Angles, in: Geernaert G.L., Plant W.L. (eds) Surface Waves and Fluxes. Environmental Fluid Mechanics, vol 8.

Wright, J., 1968. A New Model for Sea Clutter. IEEE Transactions on Antennas and Propagation 16, 217-223.

Young, I.R., Rosenthal, W., Ziemer, F., 1985a. A three-dimensional analysis of marine radar images for the determination of ocean wave directionality and surface currents. Journal of Geophysical Research: Oceans, 90, 1049-1059

Young, I.R., Rosenthal, W., Ziemer, F., 1985b. Marine radar measurements of waves and currents during turning winds. Deutsche Hydrografische Zeitschrift, 38, 23-38.

Appendix A – Differences between ADCP and Radar with depth-assimilation at Spacing 100 (200) m

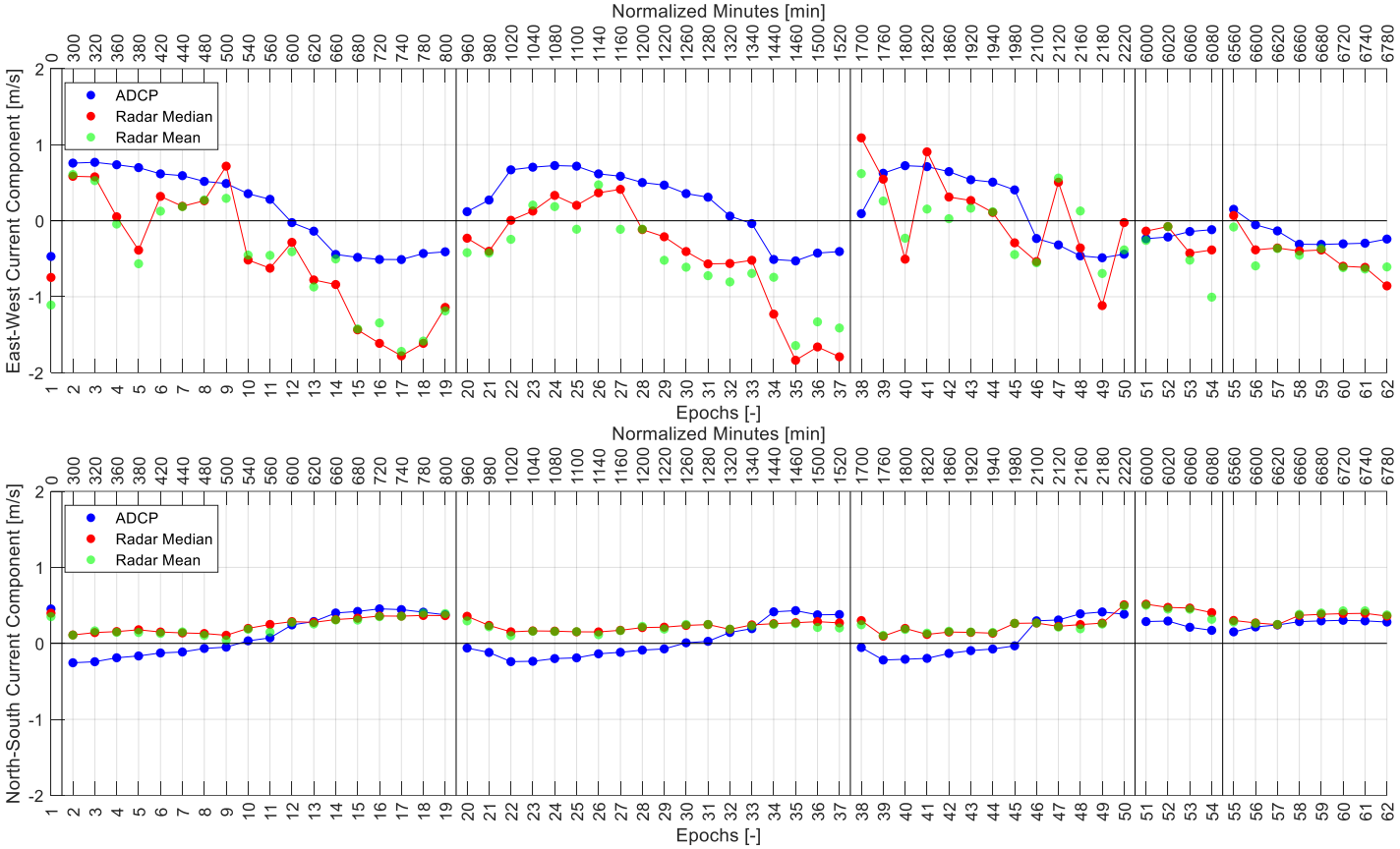

Figure A - 1 Differences between ADCP and radar in experiment 2 with 100 (200) m spacing and with depth-assimilation

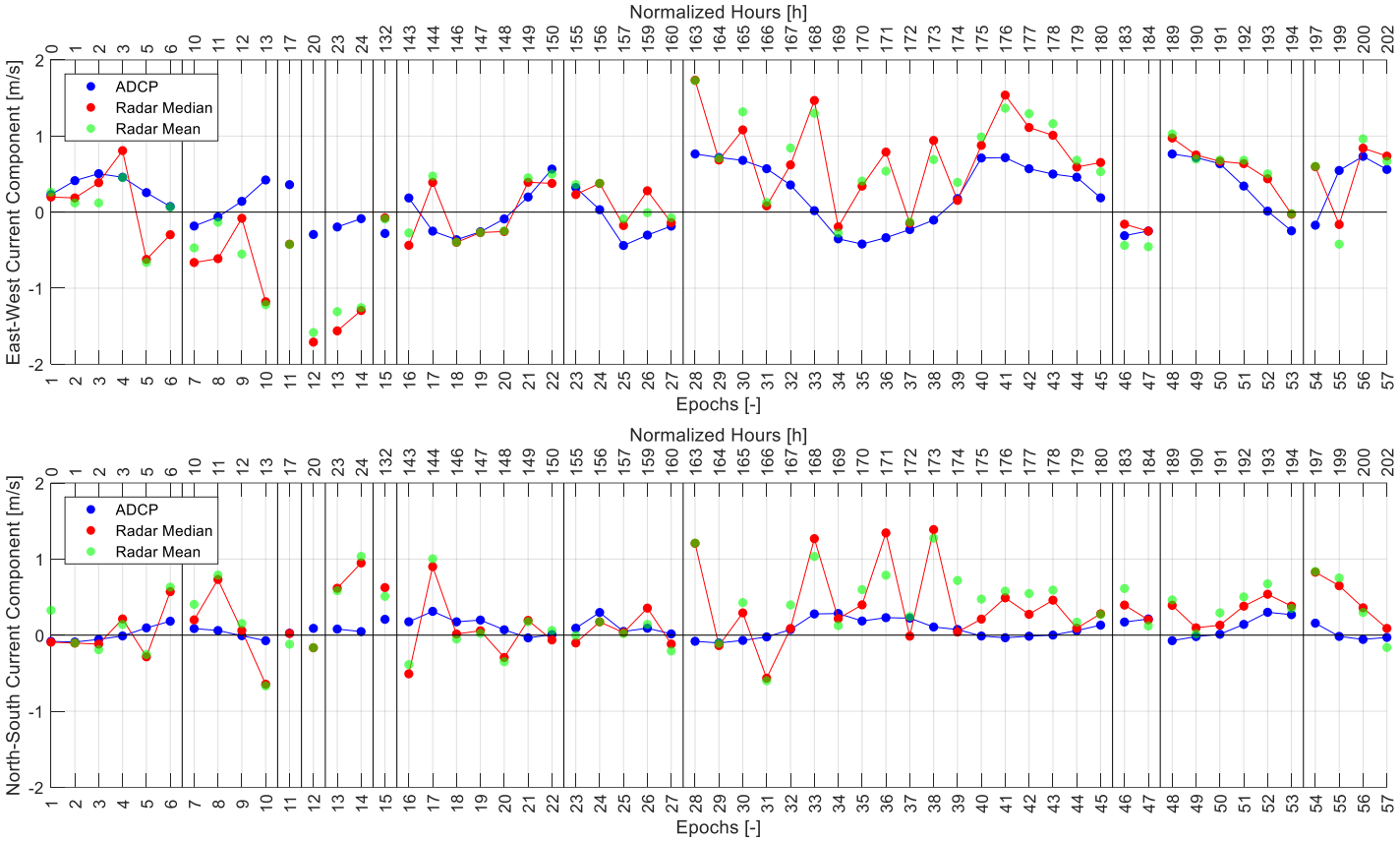

Figure A - 2 Differences between ADCP and radar in experiment 3 with 100 (200) m spacing and with depth-assimilation

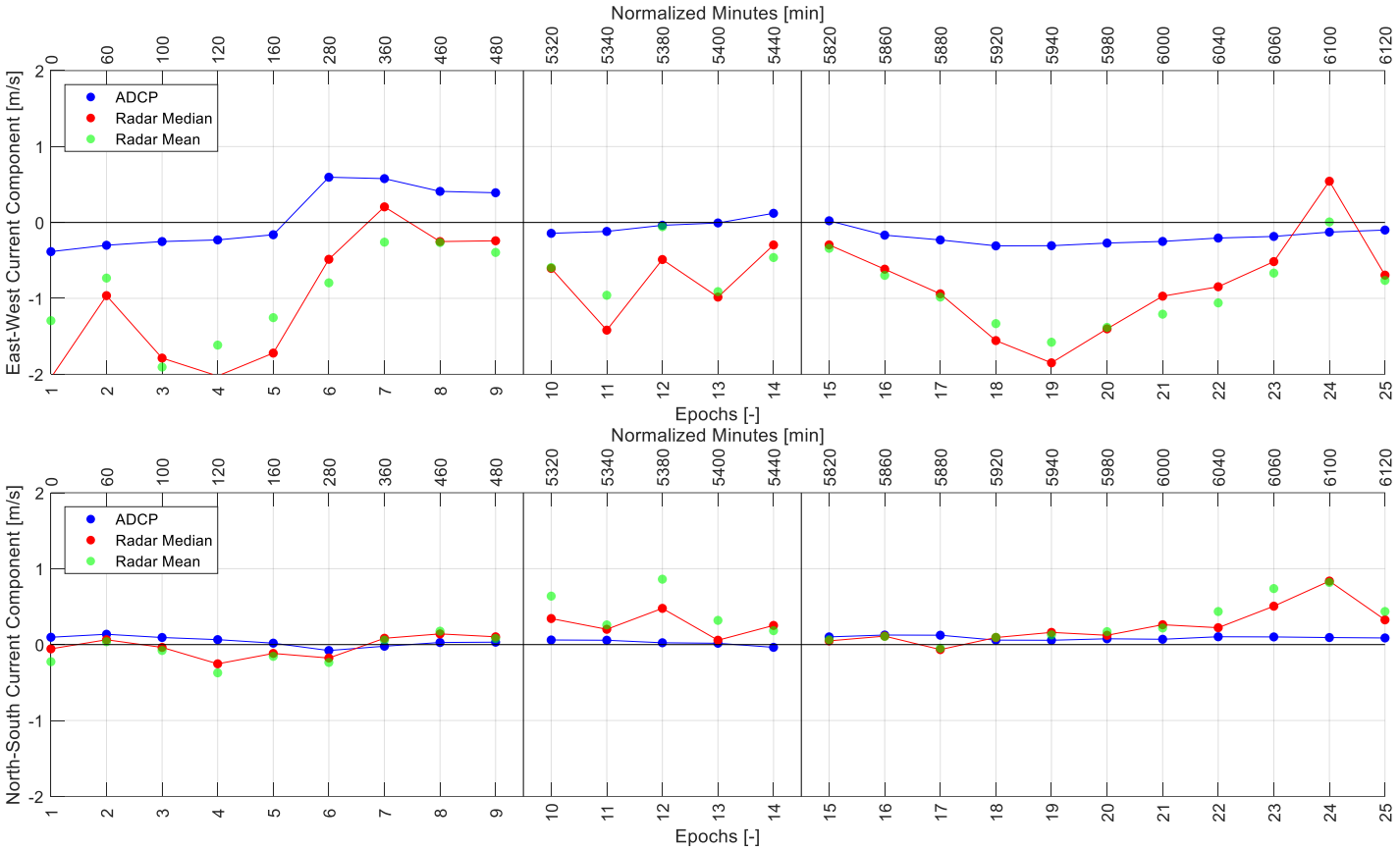

Figure A - 3 Differences between ADCP and radar in experiment 4 with 100 (200) m spacing and with depth-assimilation

Appendix B – Differences between ADCP and Radar without depth-assimilation at Spacing 100 (200) m

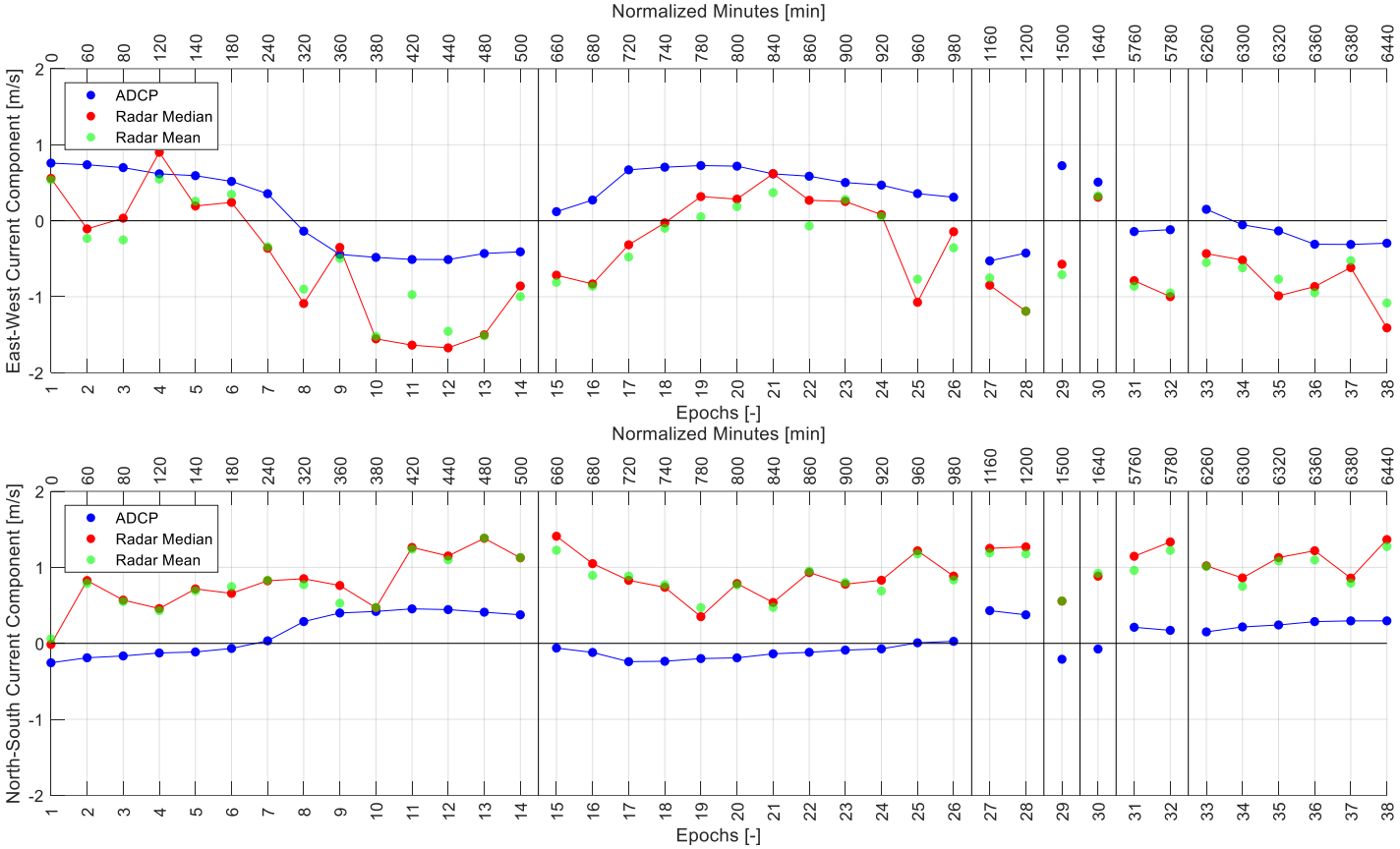

Figure B - 1 Differences between ADCP and radar in experiment 2 with 100 (200) m spacing and without depth-assimilation

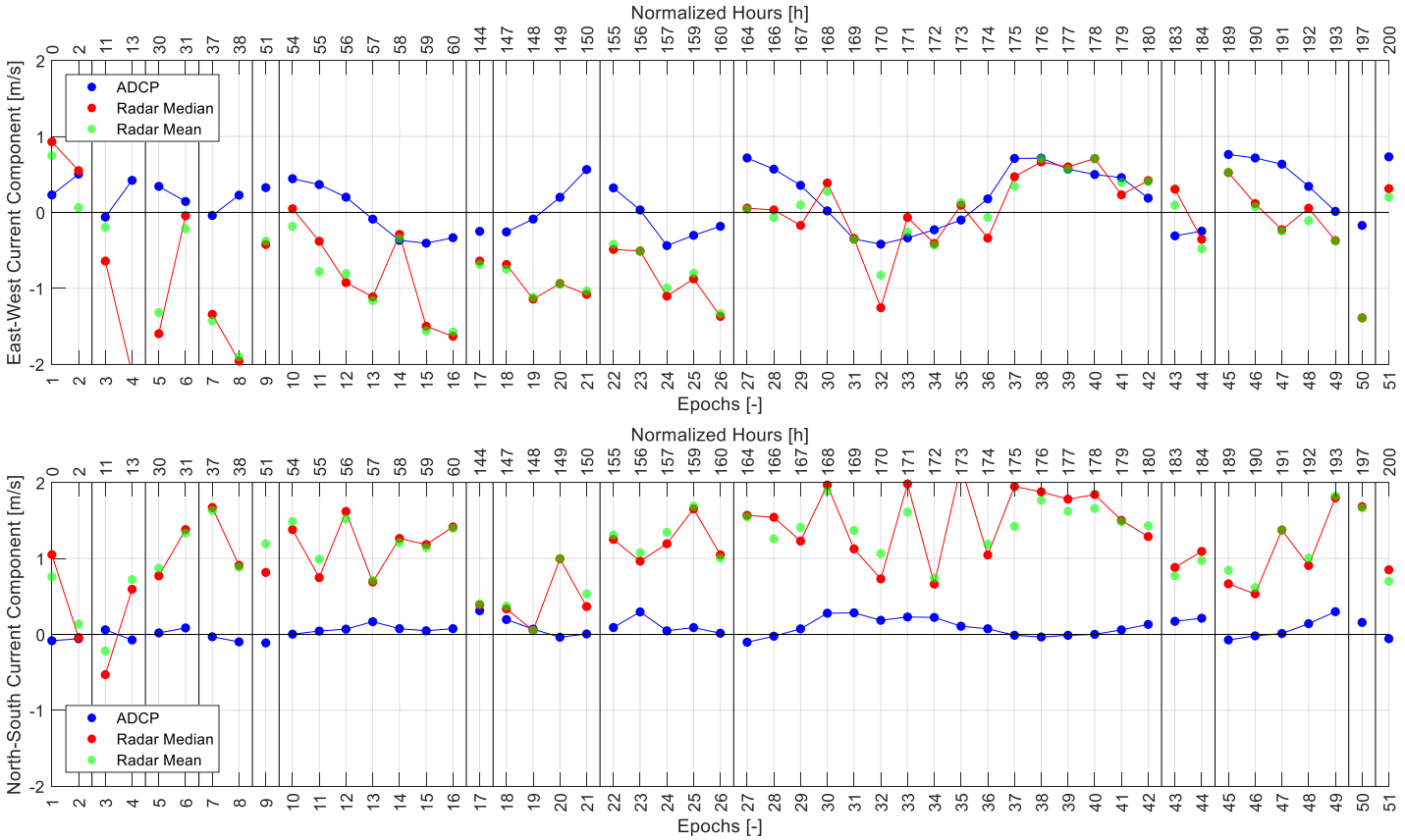

Figure B - 2 Differences between ADCP and radar in experiment 3 with 100 (200) m spacing and without depth-assimilation

Appendix C – Differences between ADCP and Radar with depth-assimilation at Spacing 500 (1000) m

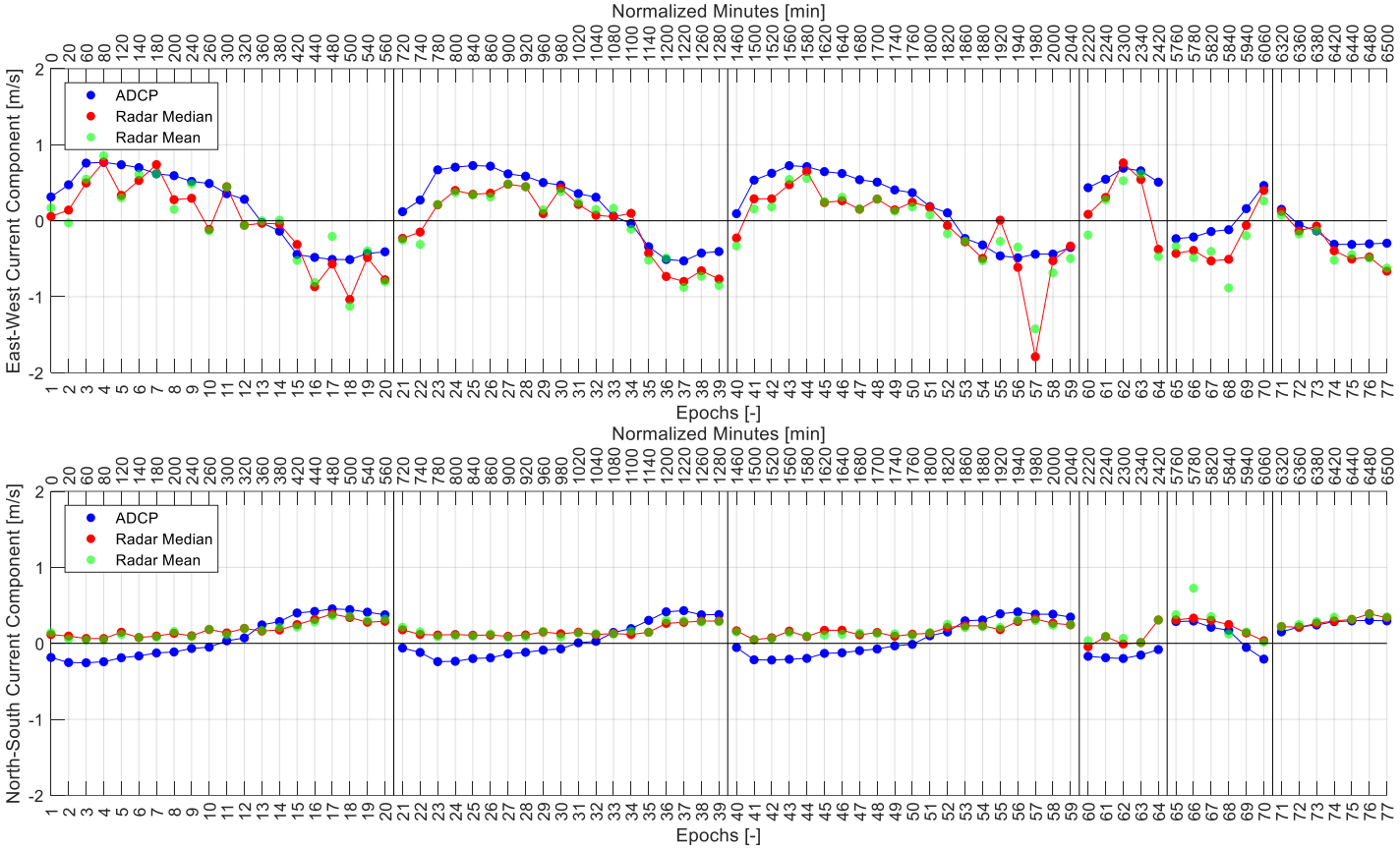

Figure C - 1 Differences between ADCP and radar in experiment 2 with 500 (1000) m spacing and with depth-assimilation

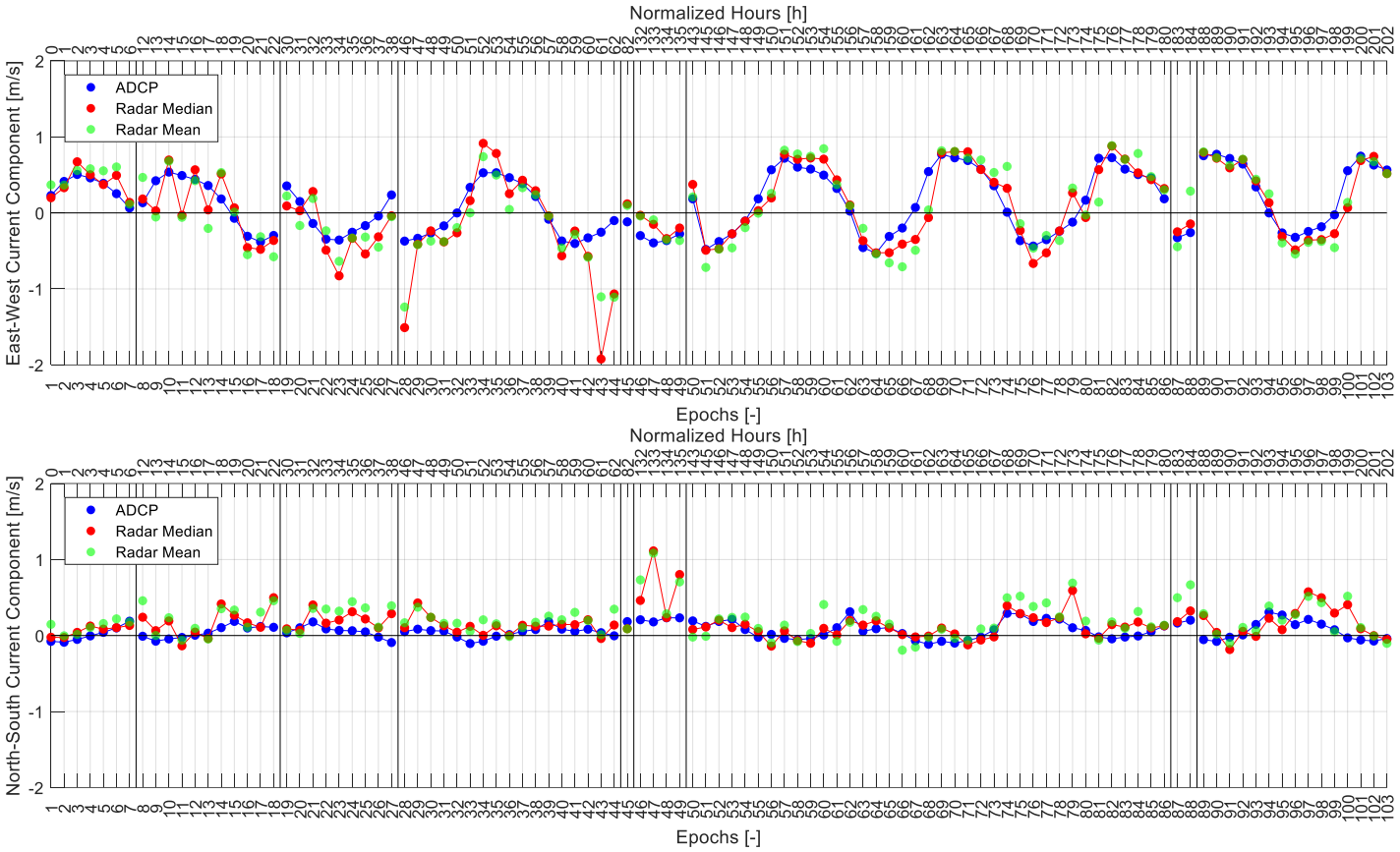

Figure C - 2 Differences between ADCP and radar in experiment 3 with 500 (1000) m spacing and with depth-assimilation

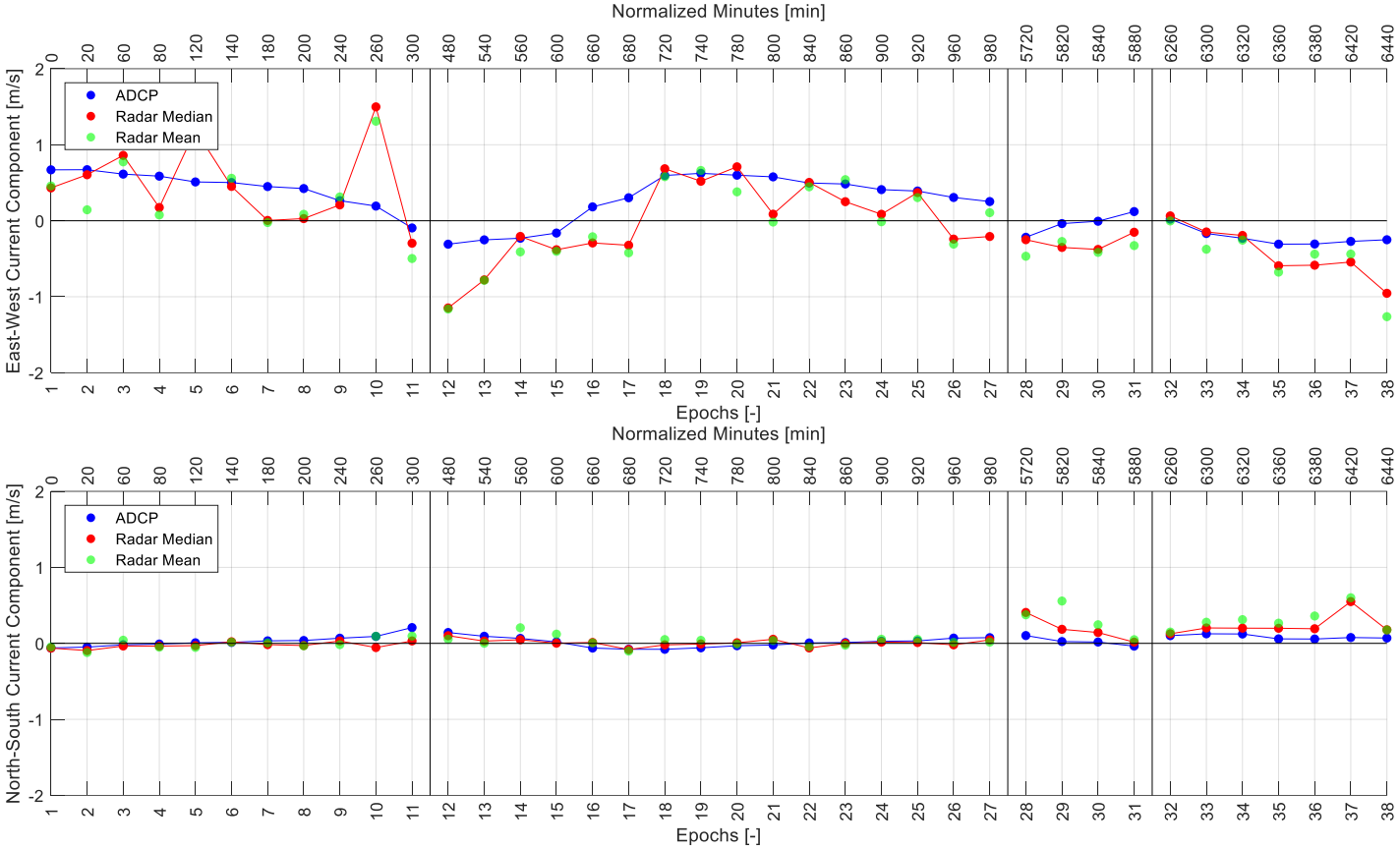

Figure C - 3 Differences between ADCP and radar in experiment 4 with 500 (1000) m spacing and with depth-assimilation

Appendix D – Differences between ADCP and Radar without depth-assimilation at Spacing 500 (1000) m

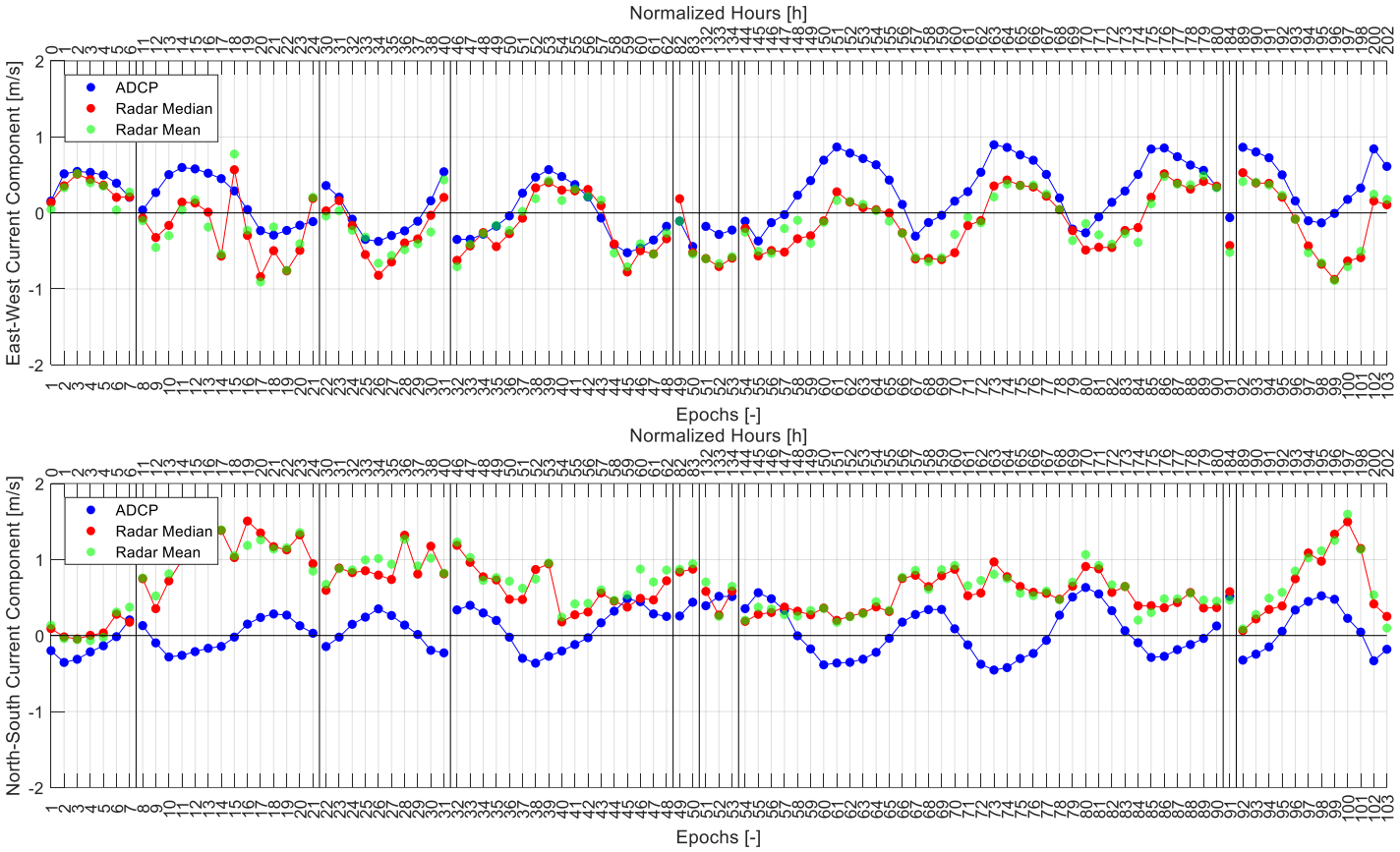

Figure D - 1 Differences between ADCP and radar in experiment 1 with 500 (1000) m spacing and without depth-assimilation

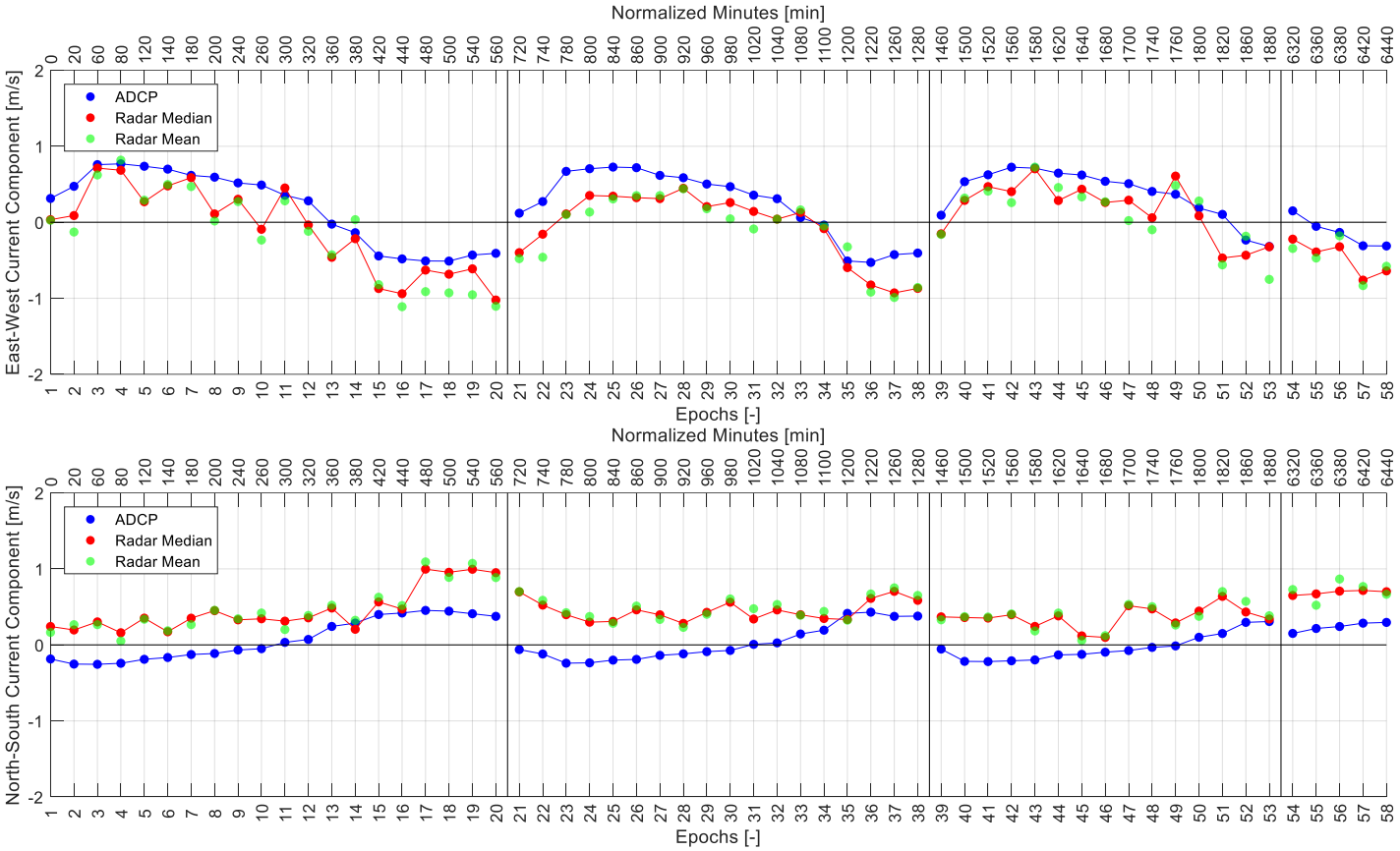

Figure D - 2 Differences between ADCP and radar in experiment 2 with 500 (1000) m spacing and without depth-assimilation

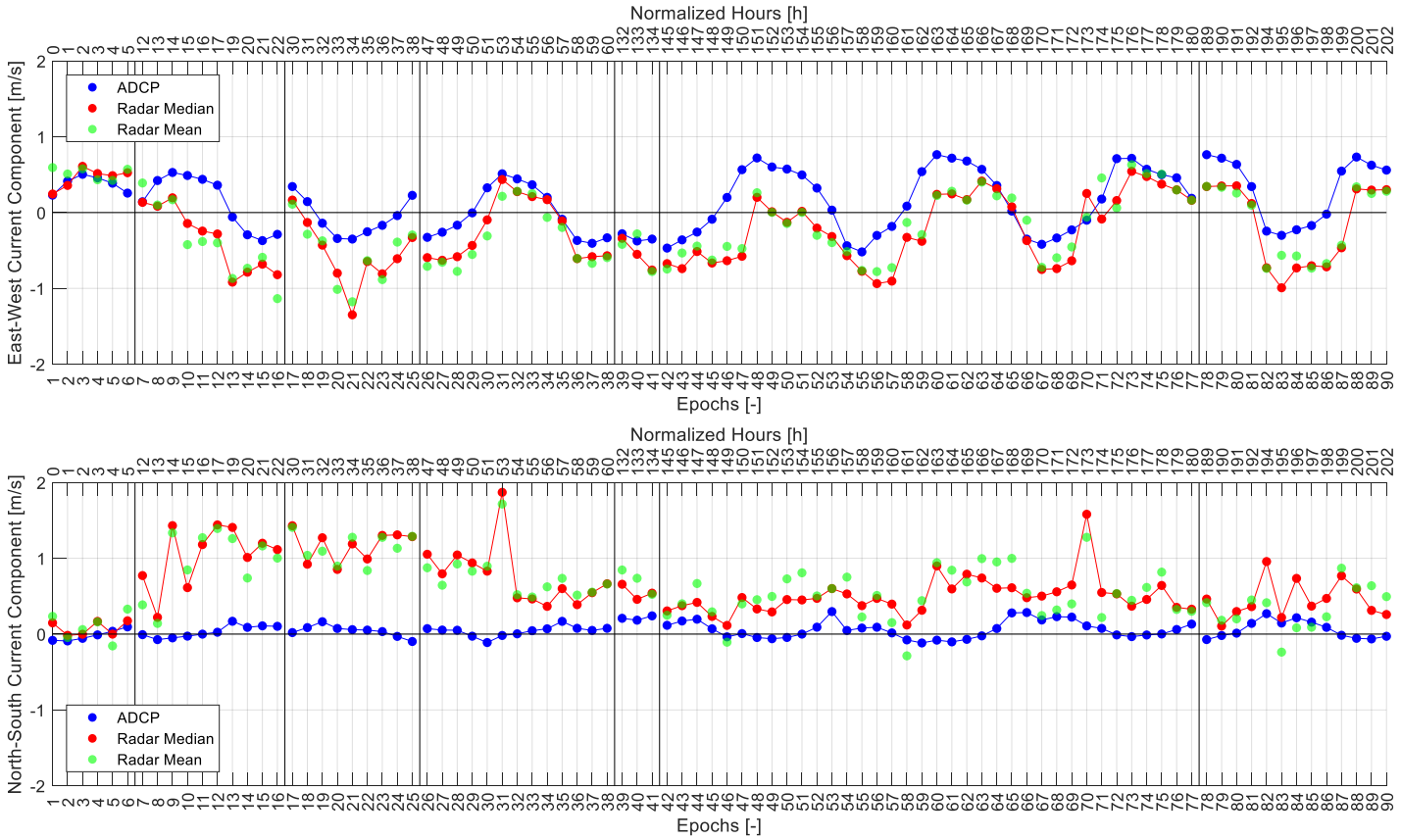

Figure D - 3 Differences between ADCP and radar in experiment 3 with 500 (1000) m spacing and without depth-assimilation

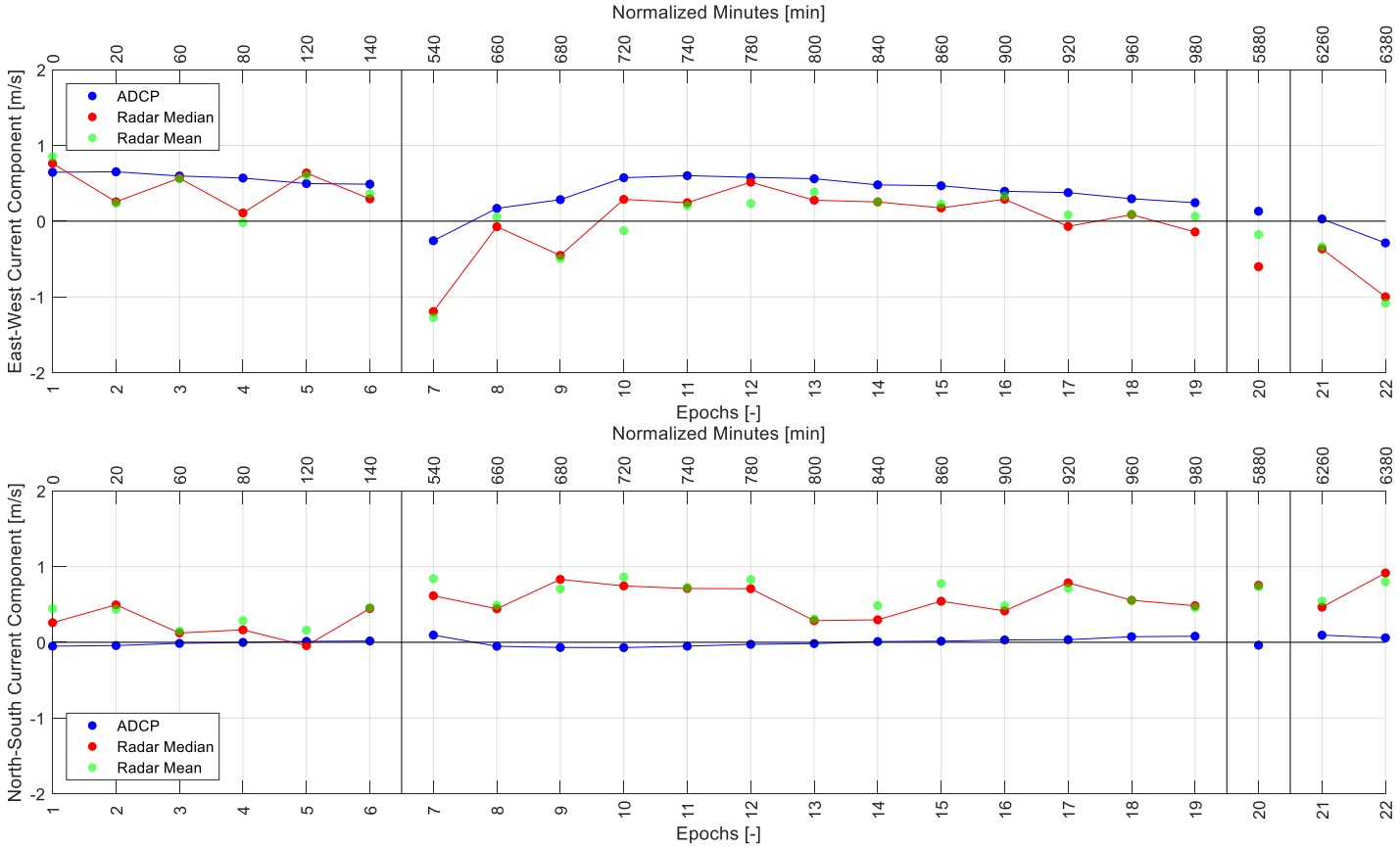

Figure D - 4 Differences between ADCP and radar in experiment 4 with 500 (1000) m spacing and without depth-assimilation.

Appendix E – Spatial Coherence with depth-assimilation at Spacing 500 (1000) m

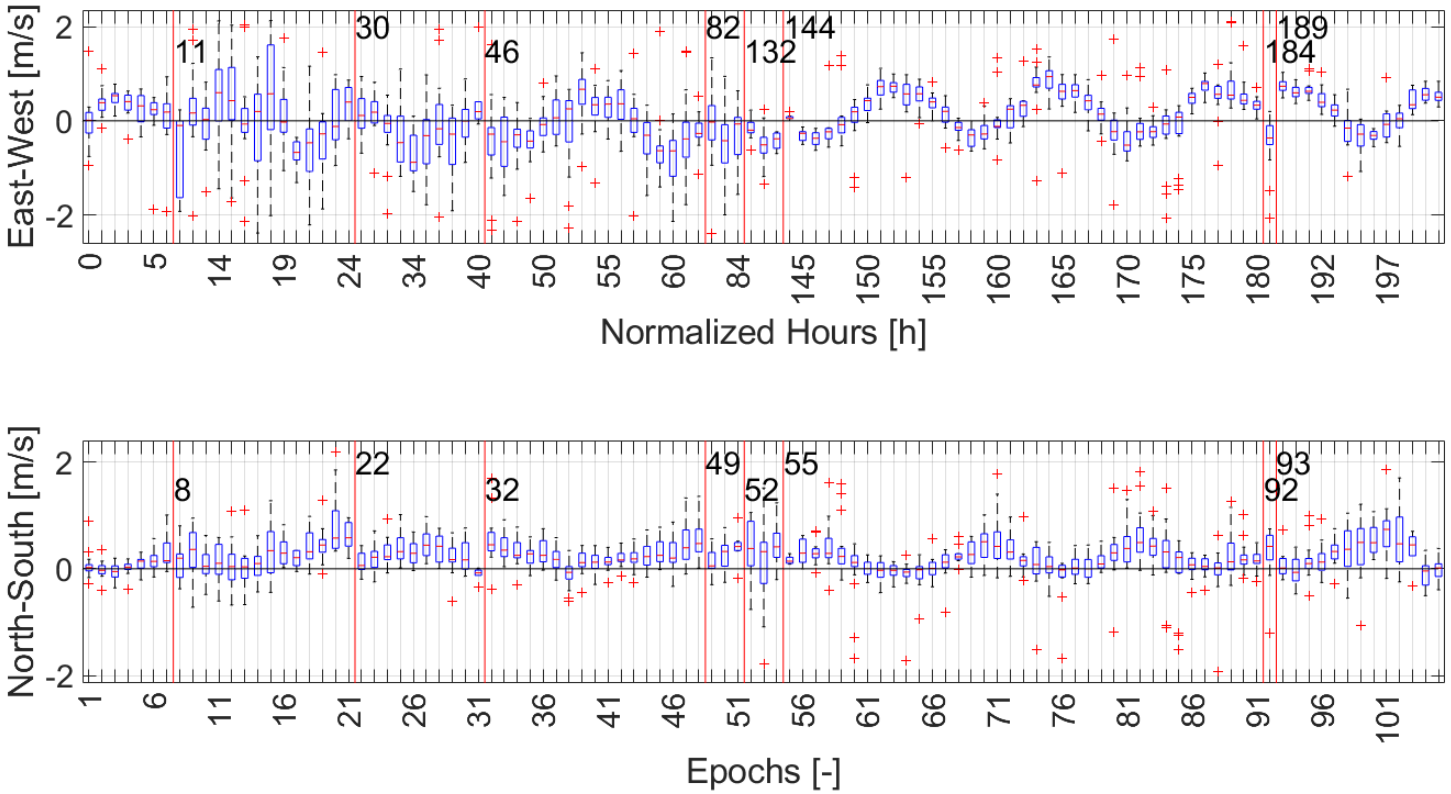

Figure E - 1 Boxplot of east-west (top) and north-south (bottom) velocity components per epoch. Red horizontal line indicating median per epoch and boxes the 25th and 75th percentiles. Outliers represented by '+' symbol and defined as more than three scaled median absolute deviations. Whiskers representing the most extreme outputs not considered outliers. X-axes corresponding to Figure 9. Good spatial coherence indicated by small boxes and small whiskers. Definitions and settings corresponding to Figure 9 but spacing of 500 (1000) m.